Initial formation of channel–shoal patterns in double–inlet systems

Deng, Xiao; De Mulder, Tom; Schuttelaars, Henk

DOI
10.1007/s10236-022-01528-6

Publication date
2022

Document Version
Final published version

Published in
Ocean Dynamics

Ocean Dynamics
https://doi.org/10.1007/s10236-022-01528-6

Initial formation of channel–shoal patterns in double–inlet systems

Xiao Deng[1] · **Tom De Mulder**[2] · **Henk Schuttelaars**[1]

Received: 30 May 2022 / Accepted: 10 October 2022

Abstract
Channel–shoal patterns are often observed in the back–barrier basins of inlet systems and are important from both an economical and ecological point of view. Focussing on double–inlet systems, the initial formation of these patterns is investigated using an idealized model. The model is governed by the depth–averaged shallow water equations, a depth–integrated concentration equation and a tidally–averaged bottom evolution equation. Focussing on rectangular basins and neglecting the effects of earth rotation, it is found that laterally uniform morphodynamic equilibria can become linearly unstable, resulting in initial patterns that resemble channels and shoals. When the water motion is only forced by an M_2 tidal constituent, the existence of (laterally uniform) morphodynamic equilibria for which both inlets are connected strongly depends on the relative phase and amplitudes of the tidal forcing. If such equilibria exist, they can be either stable against small perturbations or linearly unstable. If these equilibria are linearly unstable, two instability mechanisms can be identified, the first related to the convergences and divergences of diffusive transports, the second mechanism related to a combination of advective and diffusive transports. In the former case, all eigenvalues are real and the bedforms grow exponentially in time. In the latter case, the eigenvalues are complex, resulting in bedforms that both migrate and grow in time. In case external overtides and a time–independent discharge are included, no diffusive instabilities are found anymore for the parameters considered in this paper. This implies that all instabilities are migrating in time. In all cases considered, the bed perturbations have only an appreciable amplitude at locations where the underlying laterally uniform equilibrium has a local minimum in water depth. This is consistent with observations from numerical models and laboratory experiments.

Keywords Double–inlet systems · Morphodynamic equilibria · Linear stabilities · Channels and shoals

1 Introduction

Around 12% of the world's coastline (Mulhern et al. 2017) can be characterised as barrier coasts. They consist of barrier islands, back–barrier basins and tidal inlets connecting the back–barrier basins to the open sea (De Swart and Zimmerman 2009), and have shapes and sizes changing from place to place (Glaeser 1978; Stutz and Pilkey 2011). Barrier coasts are very important in terms of ecology and economy. They provide a habitat for many aquatic and terrestrial species and other ecosystem services, and are themselves important elements of biodiversity. They are attractive areas for economical activities such as gas–mining, dredging and recreation. Furthermore, these systems are of importance for coastal safety (Glaeser 1978). An example of a barrier coast is the Wadden Sea along the Dutch, German and Danish coast (Oost et al. 2012).

Barrier coasts are highly dynamic because of the complex interactions among water motion, sediment transport and bottom evolution and because of external changes like sea level rise and human interference (McBride et al. 1995; Van der Spek 1997). In these morphologically active areas, bottom patterns with multiple shoals separated by meandering deep channels are often observed (Dalrymple and Rhodes 1995). These channel–shoal patterns have length scales ranging from several meters to kilometers (De Swart and Zimmerman 2009). Moreover, these patterns can

Responsible Editor: Christoph Voelker

✉ Xiao Deng
dengxiaosp@163.com

Tom De Mulder
tomfo.demulder@ugent.be

Henk Schuttelaars
h.m.schuttelaars@tudelft.nl

[1] Department of Applied Mathematics, Delft University of Technology, 2628 CD, Delft, The Netherlands

[2] Hydraulics Laboratory, Department of Civil Engineering, Gent University, B-9000, Gent, Belgium

Published online: 29 November 2022

exhibit a cyclic morphodynamic evolution of several years to decades (Israel and Dunsbergen 2000).

To simulate the morphodynamic development of these channels and shoals in barrier coasts, complex process–based models were developed (Marciano et al. 2005; D'Alpaos et al. 2007; Hibma et al. 2003, 2004). For example, Van der Wegen and Roelvink (2008) simulated bottom evolution of a laterally–uniform constantly–sloping bed profile in a tidal basin. They found that channels and shoals are initiated in the shallow regions near the landward end of the tidal basin, after which these patterns branch out toward the seaward side of the tidal basin. However, the essential mechanisms that cause these bottom patterns to develop are difficult to assess from these complex state-of-the-art models.

To gain insight into the physical mechanisms initializing channel and shoal development in a single–inlet system, Schuttelaars and De Swart (1999) analyzed the linear stability of laterally uniform morphodynamic equilibria (Schuttelaars and De Swart 1996) in short basins using an idealized width–averaged model. By assuming that, tidally averaged, sediment was mainly transported by diffusive processes, they found that the basic states were unstable if the bottom friction parameter exceeded a critical value. Van Leeuwen and De Swart (2001, 2004) extended the model with internally generated advective transport. They found that channels and shoals were on the seaward boundary if the sediment transport is dominated by advective processes. Ter Brake and Schuttelaars (2011) further discussed the effect of bottom friction including topographic variations in the diffusive transport, and showed that channel–shoal patterns started to grow in the landward shallow regions.

However, these studies of channels and shoals focused on single–inlet systems, namely tidal basins with one inlet connecting to the open sea. Recent studies show that there is a strong water and sediment exchange between adjacent sub–basins in the Wadden Sea (Duran-Matute et al. 2014; Sassi et al. 2015). Such interactions are also found in the Ria Formosa in south Portugal (Salles et al. 2005; Pacheco et al. 2008) and Venice Lagoon (Seminara et al. 2005; Tambroni and Seminara 2006). This strongly suggests that to understand, model and predict the morphodynamic evolution of barrier coasts, back barrier basins should be considered as multiple–inlet systems.

The present study aims at analyzing the initial formation of channels and shoals in a double–inlet system, consisting of a basin with two inlets connecting to the open sea. Only rectangular planform geometries will be considered and the effects of earth rotation on the water motion is neglected. By studying the linear stability (Schuttelaars and De Swart 1999; Van Leeuwen and De Swart 2001; Ter Brake and Schuttelaars 2011) of laterally uniform morphodynamic equilibria in double–inlet systems (Deng et al. 2021), insight in the 2DH stability of these systems is obtained, thus extending the 1D stability analysis performed in Deng et al. (2021). Furthermore, the mechanisms resulting in these instabilities can be identified. Default parameters used are characteristic for the Marsdiep–Vlie inlet system in the Dutch Wadden Sea, even though a direct comparison with the patterns observed in this system cannot be made because of the assumption of a rectangular basin. The sensitivity of the linear stability of the basic state to tidal forcings will be investigated in detail. The linear stability analysis is a first step in systematically obtaining morphodynamic equilibria with a more complex (finite amplitude) channel–shoal structure.

In Section 2, the equations governing water motion, transport of sediment and bed evolution are presented. The scaling of the system of equations and the solution method are presented in Section 3. In Section 4, morphodynamic equilibria in double–inlet systems and their linear stability are studied. In Section 5, the results are discussed and conclusions presented.

2 Model description

We consider a rectangular tidal basin with a prescribed length L and width B (see Fig. 1a for a top view). This basin is connected to the open sea by two inlets, located at $x = 0$ and $x = L$, with x the coordinate in the along–basin (or longitudinal) direction. The landward boundaries of the rectangular tidal basin are located at $y = 0$ and $y = B$, where y is the coordinate in the cross–basin (or lateral) direction. The landward boundaries are assumed to be both impermeable for water and sediments, and non-erodible.

The free surface is located at $z = \hat{\zeta}$, measured from the undisturbed free surface found at $z = 0$ (see Fig. 1b for a side view). The undisturbed water depth of the tidal basin at $x = 0$ is denoted by H^I and at $x = L$ by H^{II}, both are assumed to be laterally uniform. The erodible bottom consisting of uniform sandy material is found at $z = \hat{h} - H^I$, where $\hat{h}$ denotes the bed level measured from the reference depth H^I. Hence, the instantaneous local water depth is given by $H^I - \hat{h} + \hat{\zeta}$.

The tidal basins we consider have a water depth much smaller than both the length and width. Hence, the water motion can be described by the depth–averaged shallow water equations for a homogeneous fluid (Csanady 1982). Assuming the basin width to be much smaller than the Rossby deformation radius allows for the neglect of earth rotation effects, resulting in the following equations:

$$\nabla \cdot [(H^I - \hat{h} + \hat{\zeta})\hat{\mathbf{u}}] + \hat{\zeta}_t = 0, \tag{1a}$$

$$\hat{\mathbf{u}}_t + \hat{\mathbf{u}} \cdot \nabla \hat{\mathbf{u}} + g \nabla \hat{\zeta} + \frac{r_* \hat{\mathbf{u}}}{H^I - \hat{h} + \hat{\zeta}} = 0, \tag{1b}$$

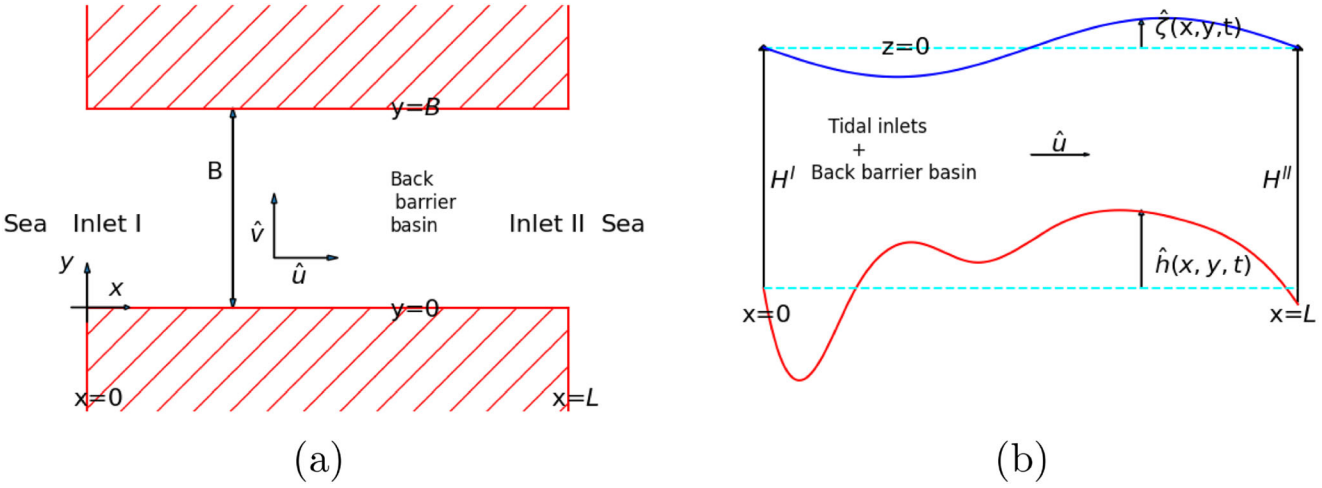

Fig. 1 A sketch of an idealized tidal basin connected to the open sea at both ends. (a) A top view of the schematized double–inlet system with a uniform width B. The longitudinal and lateral velocities are denoted by $\hat{u}$ and $\hat{v}$. (b) A longitudinal cross–section view of the double–inlet system, with the depth at inlet I denoted by H^I and the depth at inlet II denoted by $H^{I\!I}$. The bed profile (red line) is denoted by $\hat{h}(x, y, t)$, and the free surface elevation (blue line) by $\hat{\zeta}(x, y, t)$

with Eq. 1a the depth–averaged continuity equation and Eq. 1b the depth–averaged momentum equation. In these equations, the horizontal velocity is denoted by $\hat{\mathbf{u}} = (\hat{u}, \hat{v})$, with $\hat{u}$ the velocity in the longitudinal and $\hat{v}$ the velocity in lateral direction. Time is denoted by t and g denotes the gravitational acceleration. Subscripts indicate a derivative with respect to that variable, and the horizontal derivative operator is denoted as $\nabla = (\partial_x, \partial_y)$. The inner product is denoted by a dot. Following Lorentz (1922) and Zimmerman (1992), bottom friction is linearized using the bottom friction coefficient defined as $r_* = 8Uc_d/3\pi$, with U a characteristic velocity scale (which will be defined in Section 3.1) and c_d a drag coefficient.

The variables $\hat{\zeta}$ and $\hat{\mathbf{u}}$ are decomposed into a tidally–averaged and a time–varying contribution as $\hat{\zeta} = <\hat{\zeta}> + \bar{\hat{\zeta}}$ and $\hat{\mathbf{u}} = <\hat{\mathbf{u}}> + \bar{\hat{\mathbf{u}}}$, where the angular brackets $<\cdot> = \int_0^T \cdot\, dt/T$ denote the tidally averaged contribution, with T the M_2 tidal period, and an overbar $\bar{\cdot}$ the instantaneous deviation from this tidal average such that $<\bar{\cdot}> = 0$.

The time-varying parts of the sea surface elevations at the two seaward sides of the inlets are assumed to be forced by prescribed M_2 and M_4 tidal constituents,

$$\bar{\hat{\zeta}} = A^I_{M_2}\cos(\sigma t - \phi^I_{M_2}) + A^I_{M_4}\cos(2\sigma t - \phi^I_{M_4}) \text{ at } x = 0, \quad (2a)$$

$$\bar{\hat{\zeta}} = A^{I\!I}_{M_2}\cos(\sigma t - \phi^{I\!I}_{M_2}) + A^{I\!I}_{M_4}\cos(2\sigma t - \phi^{I\!I}_{M_4}) \text{ at } x = L. \quad (2b)$$

The constants $A^I_{M_2}$ ($A^I_{M_4}$) and $A^{I\!I}_{M_2}$ ($A^{I\!I}_{M_4}$) denote the amplitudes of the M_2 (M_4) tidal constituents at inlet I and $I\!I$, while the corresponding phases are denoted by $\phi^I_{M_2}$ ($\phi^I_{M_4}$) and $\phi^{I\!I}_{M_2}$ ($\phi^{I\!I}_{M_4}$). Even though these amplitudes and phases may in principle depend on the lateral coordinate y, we assume them to be uniform in the lateral direction. The angular frequency of the M_2 tidal signal is given by $\sigma = 2\pi/T$.

Furthermore, the tidally averaged mean sea surface elevation at inlet I is required to be zero and a tidally averaged discharge is prescribed at inlet $I\!I$:

$$<\hat{\zeta}> = 0 \text{ at } x = 0,\ y \in [0, B], \quad (3a)$$

$$<(H - \hat{h} - \hat{\zeta})\hat{u}> = Q_*/B \text{ at } x = L,\ y \in [0, B], \quad (3b)$$

with Q_* the residual water transport at inlet $I\!I$. A positive (negative) Q_* represents a residual water transport out of (into) the system at inlet $I\!I$. For an extensive discussion of these boundary conditions, see Deng et al. (2021).

The condition of impermeability at the landward boundaries of the back–barrier islands reads

$$(H - \hat{h} + \hat{\zeta})\hat{\mathbf{u}} \cdot \mathbf{n} = 0 \text{ at } y = 0 \text{ and } B, \quad (4)$$

in which $\mathbf{n}$ denotes the outward pointing unit vector normal to the coastline.

The sediment in the tidal basin consists of fine sand with a uniform grain size that is mainly transported as suspended load (see the scaling analysis in Section 3, the bedload transport contribution is given in Eq. 10). The associated depth–integrated concentration equation (Ter Brake and Schuttelaars 2010, 2011) reads

$$\hat{C}_t + \nabla\cdot[\hat{\mathbf{u}}\hat{C} - k_{h*}\left(\nabla\hat{C} + \frac{w_s}{k_{v*}}\beta\hat{C}\nabla\hat{h}\right)] = \alpha\hat{\mathbf{u}}\cdot\hat{\mathbf{u}} - \frac{w_s^2}{k_{v*}}\beta\hat{C}, \quad (5)$$

where $\hat{C}$ is the *depth–integrated* suspended sediment concentration. The horizontal diffusivity k_{h*}, the vertical diffusivity k_{v*}, the settling velocity w_s and the erosion parameter α (with units kgsm^{-4}) related to sediment properties (Dyer 1986) are assumed to be constant in space

and time. The deposition parameter β is defined by (see Ter Brake and Schuttelaars (2010) for details, also for the explicit expression of the settling term)

$$\beta = \frac{1}{1 - \exp(-\frac{w_s}{k_{v*}}(H^I - \hat{h} + \hat{\zeta}))}. \tag{6}$$

The boundary conditions at the two inlets read (Schuttelaars and De Swart 2000; Ter Brake and Schuttelaars 2010)

$$\lim_{k_{h*}\to 0} \hat{C}(x,t,k_{h*}) = \hat{C}(x,t,k_{h*}=0) \text{ at } x = 0 \text{ and } L, \tag{7}$$

which, based on Eq. 5, can be rewritten as

$$\hat{C}_t + \nabla\cdot(\hat{\mathbf{u}}\hat{C}) = \alpha\hat{\mathbf{u}}\cdot\hat{\mathbf{u}} - \frac{w_s^2}{k_{v*}}\beta\hat{C} \text{ at } x = 0 \text{ and } L. \tag{8}$$

At the lateral boundaries we require that there is no suspended load transport through these boundaries,

$$\left[\hat{\mathbf{u}}\hat{C} - k_{h*}\left(\nabla\hat{C} + \frac{w_s}{k_{v*}}\beta\hat{C}\nabla\hat{h}\right)\right]\cdot\mathbf{n} = 0 \text{ at } y = 0 \text{ and } B, \tag{9}$$

with $\mathbf{n}$ defined above.

The bed evolution equation (Meerman et al. 2019) is derived from the mass balance in the sediment layer and reads

$$\rho_s(1-p)\left(\hat{h}_t - \lambda\nabla^2\hat{h}\right) = -\left(\alpha\hat{\mathbf{u}}\cdot\hat{\mathbf{u}} - \frac{w_s^2}{k_{v*}}\beta\hat{C}\right). \tag{10}$$

Here, ρ_s is the sediment density and p denotes the bed porosity. The first and second term on the right–hand side of Eq. 10 model the local erosion and deposition of sediment, respectively. The first term on the left–hand side models the temporal bed changes, whereas the second term models the effects of the gravitational transport present in the bedload transport, using a highly simplified parameterisation with constant $\lambda \sim \mathcal{O}(10^{-6} - 10^{-4})\,\mathrm{m^2\,s^{-1}}$, see Schuttelaars and De Swart (1996) for a detailed discussion. Following Falqués et al. (1996) and Schuttelaars and De Swart (1999) this latter term is retained because, even though bedload transport is typically small in the systems we consider, the stabilizing effects of the slope terms may play an important role when considering the stability properties of morphodynamic equilibria.

Substituting Eq. 5 into Eq. 10 allows for rewriting the bed evolution equation as

$$\rho_s(1-p)\hat{h}_t + \hat{C}_t = -\nabla\cdot\mathbf{F}, \tag{11}$$

with

$$\mathbf{F} = \underbrace{-k_{h*}\nabla\hat{C}}_{\mathbf{F}_{\text{diff}}} \underbrace{-k_{h*}\frac{w_s}{k_{v*}}\beta\hat{C}\nabla\hat{h}}_{\mathbf{F}_{\text{topo}}} + \underbrace{\hat{\mathbf{u}}\hat{C}}_{\mathbf{F}_{\text{adv}}} \underbrace{-\rho_s(1-p)\lambda\nabla\hat{h}}_{\mathbf{F}_{\text{bed}}} \tag{12}$$

being the total depth–integrated sediment transport. This transport consists of four terms, that is a classical diffusive contribution ($\mathbf{F}_{\text{diff}}$), a topographically induced diffusive contribution ($\mathbf{F}_{\text{topo}}$), an advective contribution ($\mathbf{F}_{\text{adv}}$), and a bedload contribution ($\mathbf{F}_{\text{bed}}$).

At the seaward boundaries the depths are assumed to be fixed:

$$\hat{h} = 0 \text{ at } x = 0, \tag{13a}$$

$$\hat{h} = H^I - H^{II} \text{ at } x = L. \tag{13b}$$

Using Eq. 9, the requirement of no sediment transport through the lateral boundaries reduces to

$$\nabla\hat{h}\cdot\mathbf{n} = 0 \text{ at } y = 0 \text{ and } B, \tag{14}$$

implying no bedload transport due to slope effects is allowed through these side walls.

3 Solution method

3.1 Scaling and expansion

To assess the dominant balances in the system of equations, the equations are made dimensionless by using the following scaling:

$$(x,y) = L(\check{x},\check{y}),\ t = \sigma^{-1}\check{t},\ \hat{\mathbf{u}} = U\check{\mathbf{u}}, \tag{15a}$$

$$\hat{\zeta} = A^I_{M_2}\check{\zeta},\ \hat{h} = H^I\check{h},\ \hat{C} = \frac{\alpha U^2 k_{v*}}{w_s^2}\check{C}, \tag{15b}$$

where the dimensionless variables are indicated by a check $\check{}$. The longitudinal x and lateral coordinate y are made dimensionless by the length L of the double–inlet system (implying that $0 \le \check{y} \le B/L$), time is made dimensionless using the M_2 angular frequency σ, the surface elevation with the M_2 amplitude at the seaward side of inlet I, denoted by $A^I_{M_2}$, and the bed level is made dimensionless using the depth H^I at inlet I. The typical scale for the velocity is given by $U = A^I_{M_2}\sigma L/H^I$ (see Deng et al. (2021) for a motivation of this velocity scale). Assuming an approximate balance between erosion and deposition, the suspended sediment concentration is made dimensionless using $\alpha U^2 k_{v*}/\omega_s^2$.

Substituting these dimensionless variables in the equations and suppressing the checks, the system of equations reads (see Table 1 for a definition of the various dimensionless constants)

$$\zeta_t + \nabla\cdot[(1-h+\epsilon\zeta)\mathbf{u}] = 0, \tag{16a}$$

$$\mathbf{u}_t + \epsilon\mathbf{u}\cdot\nabla\mathbf{u} + \lambda_L^{-2}\nabla\zeta + \frac{r\mathbf{u}}{1-h+\epsilon\zeta} = 0, \tag{16b}$$

$$a[C_t + \nabla\cdot(\epsilon\mathbf{u}C - k_h\nabla C - k_h\lambda_d\beta\nabla hC)] = \mathbf{u}\cdot\mathbf{u} - \beta C, \tag{16c}$$

$$h_t + a\delta_s C_t = -\delta_s a\nabla\cdot[\epsilon\mathbf{u}C - k_h\nabla C - k_h\lambda_d\beta\nabla hC] - \delta_b\nabla h, \tag{16d}$$

Table 1 Definition of the dimensionless parameters

Parameters & Definition	
$\epsilon = \frac{A^I_{M_2}}{H^I} = \frac{U}{\sigma L}$	$\lambda_L = \frac{\sigma L}{\sqrt{H^I g}}$
$r = \frac{r_*}{H^I \sigma}$	$a = \frac{k_{v*}\sigma}{w_s^2}$
$k_h = \frac{k_{h*}}{L^2\sigma}$	$Q = \frac{Q_*}{BH^I U}$
$\delta_s = \frac{\alpha U^2}{\rho_s(1-p)H^I\sigma}$	$\delta_b = \frac{\lambda}{\sigma H^I L}$
$\lambda_d = \frac{H^I w_s}{k_{v*}}$	$\gamma = \frac{A^I_{M_4}}{A^I_{M_2}}$
$A^{II}_{r2} = \frac{A^{II}_{M_2}}{A^I_{M_2}}$	$A^{II}_{r4} = \frac{A^{II}_{M_4}}{A^I_{M_4}}$
$\Delta\phi_{M_2} = \phi^{II}_{M_2} - \phi^I_{M_2}$	$\phi^I_{r4} = \phi^I_{M_4} - 2\phi^I_{M_2}$
$\phi^{II}_{r4} = \phi^{II}_{M_4} - 2\phi^I_{M_2}$	

with the dimensionless deposition parameter β now defined as

$$\beta = \frac{1}{1 - \exp(-\lambda_d(1 - h + \epsilon\zeta))}. \tag{17}$$

The parameter $\epsilon = A^I_{M_2}/H^I$ is the ratio of the M_2 tidal amplitude to the water depth at inlet I. The parameter $\lambda_L = k_g L$ is the product of the frictionless tidal wavenumber $k_g = \sigma/\sqrt{H^I g}$ and the length of the inlet system. The dimensionless friction parameter is denoted by r and is defined as $r = r_*/H^I\sigma$. The ratio of the deposition timescale to the tidal period is denoted by $a = k_{v*}\sigma/w_s^2$, and the sediment Peclet number $\lambda_d = H^I w_s/k_{v*}$ is the ratio of the typical time it takes for a particle to settle in the water column to the typical time needed to mix particles through the water column. The dimensionless diffusion parameter is denoted by $k_h = k_{h*}/L^2\sigma$. The parameter $\delta_s = \alpha U^2/(\rho_s(1-p)H^I\sigma)$ denotes the ratio of tidal period T over the time scale related to suspended load, and $\delta_b = \lambda/\sigma H^I L$ the ratio of the tidal period T and the time scale related to the gravitational term in the bedload transport. For a definition of all parameters, see Table 1.

Both morphodynamic timescales are small: $\delta_s \ll 1$ and $\delta_b \ll 1$. Therefore, using Eq. 16d it follows that the bed changes on the tidal timescale are very small. Using a multiple timescale approach (Sanders and Verhulst 1985; Krol 1991), the evolution can be accurately approximated by considering the tidally averaged bed evolution equation:

$$h_\tau = -\nabla\cdot <\mathbf{F}>, \tag{18}$$

$$\text{with} \quad \mathbf{F} = \underbrace{-ak_h\nabla C}_{\mathbf{F}_{\text{diff}}} \underbrace{-ak_h\lambda_d\beta C\nabla h}_{\mathbf{F}_{\text{topo}}} + \underbrace{a\epsilon\mathbf{u}C}_{\mathbf{F}_{\text{adv}}} \underbrace{-\frac{\delta_b}{\delta_s}\nabla h}_{\mathbf{F}_{\text{bed}}},$$

with $\tau = \delta_s t$ the long (morphodynamic) timescale, i.e., the timescale at which the bed changes are significant.

The associated dimensionless boundary conditions read

$$\zeta = \cos t + \gamma\cos(2t - \phi^I_{r4}) \text{ at } x = 0, \tag{19a}$$

$$\bar{\zeta} = A^{II}_{r2}\cos(t - \Delta\phi_{M_2}) + \gamma A^{II}_{r4}\cos(2t - \phi^{II}_{r4}) \text{ at } x = 1, \tag{19b}$$

$$<(1 - h + \epsilon\zeta)u> = Q \text{ at } x = 1, \tag{19c}$$

$$(1 - h + \epsilon\zeta)\mathbf{u}\cdot\mathbf{n} = 0 \text{ at } y = 0, B/L, \tag{19d}$$

$$<\mathbf{u}\cdot\mathbf{u} - \beta C> = 0 \text{ at } x = 0, 1, \tag{19e}$$

$$\lim_{k_h\to 0}\bar{C}(x, t, k_h) = \bar{C}(x, t, k_h = 0) \text{ at } x = 0, 1 \tag{19f}$$

$$(\epsilon\mathbf{u}C - k_h\nabla C - k_h\lambda_d C\nabla h)\cdot\mathbf{n} = 0 \text{ at } y = 0, B/L, \tag{19g}$$

$$h = 0 \text{ at } x = 0, \tag{19h}$$

$$h = 1 - \frac{H^{II}}{H^I} \text{ at } x = 1, \tag{19i}$$

$$\nabla h\cdot\mathbf{n} = 0 \text{ at } y = 0, B/L. \tag{19j}$$

Here, the parameter γ is the ratio of the amplitudes of the M_4 and M_2 tidal constituents at inlet I, and $A^{II}_{r2} = A^{II}_{M_2}/A^I_{M_2}$ ($A^{II}_{r4} = A^{II}_{M_4}/A^I_{M_4}$) the ratio of the amplitudes of the M_2 (M_4) tide at inlet II and at inlet I. The parameter $\Delta\phi_{M_2} = \phi^{II}_{M_2} - \phi^I_{M_2}$ is the phase difference between the M_2 tide at inlet II and at inlet I. The relative phases at inlets I and II are defined as $\phi^I_{r4} = \phi^I_{M_4} - 2\phi^I_{M_2}$ and $\phi^{II}_{r4} = \phi^{II}_{M_4} - 2\phi^I_{M_2}$. The dimensionless residual water transport at inlet II is denoted by $Q = Q_*/(BH^I U)$ and is assumed to be of order ϵ.

For the systems we consider, the parameters ϵ and γ are much smaller than 1 (see Table 2 for a typical example), allowing for the introduction of an asymptotic expansion in ϵ and γ of the physical variables $\Phi \in \{\zeta, u, v, C\}$,

$$\Phi = \Phi^{00} + \epsilon\Phi^{10} + \gamma\Phi^{01} + \text{h.o.t.}, \tag{20}$$

where the first superscript denotes the order in ϵ while the second one denotes the order in γ. Substituting this asymptotic expansion in Eqs. 16a–16c, 18 and the boundary conditions (3.1), these equations are ordered with respect to the small parameters ϵ and γ. For the leading order morphodynamic balance, it turns out that only the leading order and first order contributions of the water motion and concentration equation in ϵ and γ have to be solved for. The time dependency of the various physical variables can be written as an (infinite) sum of tidal constituents and a residual component,

$$\Phi^{ij}(x, y, t) = \Phi^{ij}_{\text{res}}(x, y) + \sum_{k=1}^{\infty}\Phi^{ij}_{ck}(x, y)\cos kt + \sum_{k=1}^{\infty}\Phi^{ij}_{sk}(x, y)\sin kt, \tag{21}$$

Table 2 Characteristic values representative for the Marsdiep-Vlie inlet system (Ridderinkhof 1988; Duran-Matute et al. 2014). In the experiments in this paper, the depth at inlet *II* is taken to be 11.7 m, a rectangular inlet system is used with a uniform width of 6 km. This results in $l_n = 30.9n$

Quantities in the dimensional model	
System	Sediment & Bed
$L = 59\,\mathrm{km}$	$k_{h*} = 10^2\,\mathrm{m^2\,s^{-1}}$
$g = 9.81\,\mathrm{m\,s^{-2}}$	$\alpha = 0.5 \cdot 10^{-2}\ \mathrm{kg\,s\,m^{-4}}$
$c_d = 0.0025$	$\lambda \sim 10^{-6} - 10^{-4}\,\mathrm{m^2\,s^{-1}}$
$\sigma = 1.4 \cdot 10^{-4}\,\mathrm{s^{-1}}$	$k_{v*} = 0.1\,\mathrm{m^2\,s^{-1}}$
$T = 44.9 \cdot 10^3\,\mathrm{s}$	$d_{50} = 2 \cdot 10^{-4}\,\mathrm{m}$
$Q_* = -900\,\mathrm{m^3 s^{-1}}$	$\rho_s = 2650\,\mathrm{kg\,m^{-3}}$
	$p = 0.4$
	$w_s = 0.015\,\mathrm{m\,s^{-1}}$
Inlet specific parameters	
Marsdiep Inlet	Vlie Inlet
$H^I = 11.7\,\mathrm{m}$	$H^{II} = 11.9\,\mathrm{m}$
$A^I_{M_2} = 0.62\,\mathrm{m}$	$A^{II}_{M_2} = 0.77\,\mathrm{m}$
$\phi^I_{M_2} = 148°$	$\phi^{II}_{M_2} = -158°$
$B^I = 5.954\,\mathrm{km}$	$B^{II} = 5.619\,\mathrm{km}$
$A^I_{M_4} = 0.11\,\mathrm{m}$	$A^{II}_{M_4} = 0.06\,\mathrm{m}$
$\phi^I_{M_4} = 155°$	$\phi^{II}_{M_4} = -121°$
Quantities in the non–dimensional model	
$\epsilon = 5.30 \cdot 10^{-2}$	$\lambda_L = 0.77$
$r = 5.67 \cdot 10^{-1}$	$a = 6.22 \cdot 10^{-2}$
$k_h = 2.05 \cdot 10^{-4}$	$Q = -2.95 \cdot 10^{-2}$
$\delta_s = 3.68 \cdot 10^{-4}$	$\delta_b \sim 10^{-8} - 10^{-6}$
$\lambda_d = 1.75$	$\gamma = 1.83 \cdot 10^{-1}$
$A^{II}_{r2} = 1.25$	$A^{II}_{r4} = 0.535$
$\Delta\phi_{M_2} = 54°$	$\phi^I_{r4} = -141°$
$\phi^{II}_{r4} = -57°$	

where the subscript 'res' denotes the tidally–averaged contribution to the variable $\Phi(x, y, t)$, and the contributions that temporally vary as cosines (sines) with frequency k are denoted with the subscript ck (sk). The superscript i denotes the order in ϵ and the second superscript j the order in γ.

By using the specific forcing of the water motion prescribed at the inlets, it follows that the temporal variations of the physical variables are restricted to only a few tidal constituents. This can be seen by substituting the Fourier expansion Eq. 21 in the system of equations (16). Next collecting terms of the same order in ϵ and γ and of same tidal constituent, using the prescribed boundary conditions, it is found that the water motion consists in leading order of an M_2 tidal constituent only, at order ϵ a residual and M_4 contributions are generated, while M_4 contributions are found at order γ:

$$\begin{aligned}
&\mathbf{u}(x, y, t)\\
&= \mathbf{u}^{00}_{c1}(x, y)\cos(t) + \mathbf{u}^{00}_{s1}(x, y)\sin(t)\\
&\quad +\epsilon\left[\mathbf{u}^{10}_{\mathrm{res}}(x, y) + \mathbf{u}^{10}_{c2}(x, y)\cos(2t) + \mathbf{u}^{10}_{s2}(x, y)\sin(2t)\right]\\
&\quad +\gamma\left[\mathbf{u}^{01}_{c2}(x, y)\cos(2t) + \mathbf{u}^{01}_{s2}(x, y)\sin(2t)\right].
\end{aligned} \tag{22}$$

This expansion is the same for the sea surface elevation $\zeta(x, y, t)$. These water motion components are found as forcing terms in the ordered concentration equation. At leading order, a residual and M_4 concentrations are generated. At order ϵ and γ only the M_2 concentrations are calculated, as the concentration that varies with the M_6 tidal frequency does not result in residual sediment transport at leading order. The expansion of $C(x, y, t)$ reads

$$\begin{aligned}
&C(x, y, t)\\
&= C^{00}_{\mathrm{res}}(x, y) + C^{00}_{c2}(x, y)\cos(2t) + C^{00}_{s2}(x, y)\sin(2t)\\
&\quad +\epsilon\left[C^{10}_{c}(x, y)\cos(t) + C^{10}_{s}(x, y)\sin(t)\right]\\
&\quad +\gamma\left[C^{01}_{c}(x, y)\cos(t) + C^{01}_{s}(x, y)\sin(t)\right].
\end{aligned} \tag{23}$$

Using these expressions, the leading order tidally–averaged sediment transport contributions are given by

$$<\mathbf{F}^{00}_{\mathrm{diff}}> = -ak_h\nabla C^{00}_{\mathrm{res}}, \tag{24}$$

$$<\mathbf{F}^{00}_{\mathrm{topo}}> = -ak_h\beta\lambda_d C^{00}_{\mathrm{res}}\nabla h, \tag{25}$$

$$\begin{aligned}
<\mathbf{F}^{20}_{\mathrm{adv}}> = &\frac{1}{2}a\epsilon^2(\mathbf{u}^{00}_{c1}C^{10}_{c1} + \mathbf{u}^{00}_{s1}C^{10}_{s1} + 2\mathbf{u}^{10}_{\mathrm{res}}C^{00}_{\mathrm{res}}\\
&+ \mathbf{u}^{10}_{c2}C^{00}_{c2} + \mathbf{u}^{10}_{s2}C^{00}_{s2}),
\end{aligned} \tag{26}$$

$$\begin{aligned}
<\mathbf{F}^{11}_{\mathrm{adv}}> = &\frac{1}{2}a\epsilon\gamma(\mathbf{u}^{00}_{c1}C^{01}_{c1} + \mathbf{u}^{00}_{s1}C^{01}_{s1} + \mathbf{u}^{01}_{c2}C^{00}_{c2}\\
&+ \mathbf{u}^{01}_{s2}C^{00}_{s2}),
\end{aligned} \tag{27}$$

$$<\mathbf{F}_{\mathrm{bed}}> = -\frac{\delta_b}{\delta_s}\nabla h, \tag{28}$$

in which $\mathbf{F}^{00}_{\mathrm{diff}}$ is the classical diffusive contribution and $\mathbf{F}^{00}_{\mathrm{topo}}$ is the topographically induced diffusive contribution. The advective transport is decomposed in two contributions, the internally generated advection denoted as $\mathbf{F}^{20}_{\mathrm{adv}}$ and the externally generated advection denoted as $\mathbf{F}^{11}_{\mathrm{adv}}$. The transport due to the gravitational effect of bedload is denoted by $\mathbf{F}_{\mathrm{bed}}$. This term is always much smaller than the topographically induced diffusive contribution (Hepkema et al. 2019) and will be added to the topographically induced diffusive transport when plotting the various contributions.

3.2 Basic state and linear stability

The resulting system of morphodynamic equations, ordered in terms of the small parameters and expanded in tidal constituents, can be written as

$$K\Psi_\tau = G(\boldsymbol{\Psi}), \tag{29}$$

where Ψ is a 29–dimensional vector of the amplitudes of all physical variables considered. Namely, $\Psi = (\zeta_{c1}^{00}, \zeta_{s1}^{00}, \zeta_{res}^{10}, \zeta_{c2}^{10}, \zeta_{s2}^{10}, \zeta_{c2}^{01}, \zeta_{s2}^{01}, ..., h)$, where the dots indicate the amplitudes of the longitudinal velocity u, lateral velocity v and concentration C. The matrix K is a diagonal matrix, with a non–zero element (equal to one) only at the row associated with the bed evolution equation and G is a nonlinear operator working on the vector Ψ.

For a double inlet system with a *rectangular* geometry and in which the forcing due to the earth rotation is neglected, the system of equations (29) allows for morphodynamic equilibria $\boldsymbol{\Psi}_\mathrm{e} = \Psi_e(x)$ that are laterally uniform and satisfy

$$G(\boldsymbol{\Psi}_\mathrm{e}) = 0. \tag{30}$$

These morphodynamic equilibria do not depend on the lateral coordinate y and the amplitudes of the lateral velocities considered are zero. To obtain these basic states $\boldsymbol{\Psi}_\mathrm{e}$, the system of equations is first discretized using a finite element method with continuous Langrange elements. The number of elements used in the longitudinal direction is 800 (increasing the number of elements resulting in small relative changes, typically smaller than 0.01 in the amplitudes, not shown) with the degree of each element 2, resulting in a total number of degrees of freedom of 46429. Next, a Newton–Raphson iterative method is employed to numerically find the solution of Eq. 30, see Deng et al. (2021) for a detailed discussion.

These laterally uniform morphodynamic equilibria can be unstable against both one dimensional (laterally uniform) and two–dimensional perturbations (perturbations with lateral structure). To assess this stability for small perturbations, an infinitesimally small two–dimensional perturbation is added to the basic state $\boldsymbol{\Psi}_\mathrm{e}$,

$$\boldsymbol{\Psi}(x, y, \tau) = \Psi_\mathrm{e}(x) + \Psi'(x, y, \tau), \tag{31}$$

which is then inserted into Eq. 29. Since the perturbations are small, only terms linear in these perturbations are retained. The resulting linearized equations allow for a solution using the ansatz

$$\boldsymbol{\Psi}' = \Re\left[\hat{\boldsymbol{\Psi}}'(x, y)\exp(\omega\tau)\right],$$

with $\Re(\omega)$ giving the real part of ω, indicating the exponential growth rate. The imaginary part of ω, given by $\Im(\omega)$, gives the frequency. Substituting this ansatz results in the following eigenvalue problem

$$\omega K\hat{\boldsymbol{\Psi}}' = L(\boldsymbol{\Psi}_\mathrm{e})\hat{\boldsymbol{\Psi}}', \tag{32}$$

with L the Jacobian matrix associated with the operator G, evaluated at $\boldsymbol{\Psi}_\mathrm{e}$ (The associated eigenvalue problem is discretized using the same method as used in the equilibrium problem). Note that the linear stability analysis only gives information of the patterns that might start to develop on the laterally uniform equilibrium, no information concerning the final bathymetry can be directly inferred from this analysis. In the system we consider, the lateral structure of the various components of the eigenvector $\hat{\boldsymbol{\Psi}}'$ can be inferred from the boundary conditions, resulting in:

$$\begin{aligned}
&\hat{u}'(x, y) = u_n'(x)\cos(l_n y), \quad \hat{v}'(x, y) = v_n'(x)\sin(l_n y),\\
&\hat{\zeta}'(x, y) = \zeta_n'(x)\cos(l_n y), \quad \hat{C}'(x, y) = C_n'(x)\cos(l_n y),\\
&\hat{h}'(x, y) = h_n'(x)\cos(l_n y).
\end{aligned}$$

The longitudinal structure of the eigenfunctions is indicated by $\cdot'$ and the dimensionless wave number l_n is defined by

$$l_n = n\pi L/B, \quad n = 0, 1, 2, \ldots, \tag{33}$$

with n the lateral mode number. When $n = 0$, the eigenpatterns are laterally uniform and the associated eigenvalues determine stability against perturbations without any lateral structure. For $n \neq 0$, the eigenpatterns are laterally varying and the eigenvalues determine the stability of the laterally uniform morphodynamic equilibria against laterally varying perturbations.

4 Results

The linear stability of laterally uniform morphodynamic equilibria is investigated and the associated instability mechanisms are discussed. In Section 4.1, the water motion in the double inlet system is only forced by a prescribed M_2 tidal forcing at both inlets. Subsequently, the influence of prescribed external overtides and discharge are elaborated upon in Section 4.2. All results are obtained using parameter values that are representative of the Marsdiep–Vlie inlet system (see Table 2), unless mentioned otherwise. A uniform width B of 6 km is considered in all experiments. Furthermore, since the undisturbed water depths at both inlets, H^I and H^{II}, are very close together, they are for simplicity both taken to be equal to 11.7 m. Hence, the dimensionless boundary condition Eq. 19i reduces to $h = 0$ at $x = 1$.

4.1 M_2 tidal forcing

In this section, the water motion is only forced by prescribed M_2 tidal amplitudes and phases at inlets I and II, while the amplitudes of the externally prescribed overtides ($A^{I}_{M_4}$ and $A^{II}_{M_4}$) and the discharge Q at inlet II are assumed to be zero. With this forcing, the sediment is transported due to diffusive processes (both the standard diffusive process and the one related to the topographic variations), advective transports related to the internally generated overtides and the bedload transport. Hence, the bottom evolution equation (18) reduces to

$$h_\tau = -\nabla \cdot \left(<\mathbf{F}^{00}_{\text{diff}}> + <\mathbf{F}^{00}_{\text{topo}}> + <\mathbf{F}^{20}_{\text{adv}}> + <\mathbf{F}_{\text{bed}}> \right),$$

with the various transport terms defined in Eqs. 24–26 and 28.

To systematically investigate the influence of the M_2 tidal forcing on the linear stability of associated laterally uniform equilibria, we first have to obtain these underlying equilibria using the bifurcation approach discussed in Deng et al. (2021). In this approach, the system of morphodynamic equations is averaged over the width and morphodynamic solutions that do not vary on the long timescale are directly searched for using a continuation procedure (for details, see Deng et al. (2021)). In Fig. 2a the minimum water depth WD_{min} of the resulting equilibrium is shown as a function of the relative phase between inlet I and II, $\Delta\phi_{M_2}$, that is varied between $-60°$ and $60°$. The distance from inlet I where WD_{min} is observed is color coded. In this experiment, the M_2 amplitudes have their prescribed values.

From these results it follows that the number of morphodynamic equilibria and their linear stability to one–dimensional perturbations (denoted as 1D–stability) strongly depend on the relative phase: for $\Delta\phi_{M_2}$ between $-2°$ and $-14°$ (indicated by the labels $L2$ and $L1$, respectively) no morphodynamic equilibrium is found for which both inlets are connected. For the other phases considered, there is always one 1D–stable equilibrium (indicated by the solid line), while for most phases also a 1D–unstable equilibrium exists (dotted line).

The 1D–stable morphodynamic equilibria are not necessarily 2D–stable, i.e. linearly stable against perturbations with a lateral structure. To illustrate this, we consider three morphodynamic solutions that are stable against one–dimensional perturbations, obtained with $\Delta\phi_{M_2} = -11°$, $\Delta\phi_{M_2} = 15°$ and $\Delta\phi_{M_2} = 19°$ (see the orange, blue and green crosses in Fig. 2a, with the laterally uniform equilibrium beds shown in Fig. 2b).

In Fig. 3a (Fig. 3b) the real (imaginary) part of the eigenvalue of the most unstable eigenfunction is shown as a function of the lateral wavenumber $l_n = n\pi L/B$ for three relative phases:

- $\Delta\phi_{M_2} = -11°$ (orange lines in Fig. 3): all eigenvalues are real. Eigenpatterns associated with $l_n \lesssim 100$ and $l_n \gtrsim 1010$ are linearly stable, for $100 \lesssim l_n \lesssim 1010$ the eigenmodes are linearly unstable. The maximum growth rate is found for $l_n \approx 550$. The longitudinal structure of the most unstable eigenmode is shown in Fig. 3c, indicating that the bed perturbations are nonzero within a region of ~ 10 km around the location where the water depth of the underlying equilibrium is minimal. The spatial structure of the most unstable bed perturbation superposed on the laterally uniform underlying morphodynamic equilibrium is illustrated in

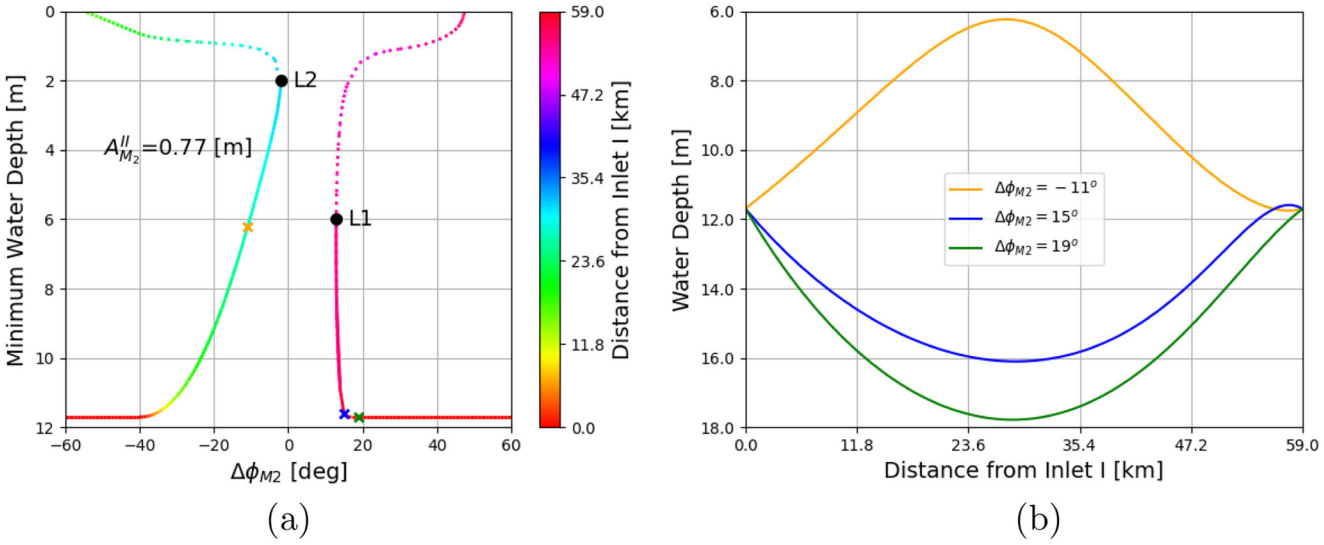

Fig. 2 Laterally uniform morphodynamic equilibria when taking diffusive and internally generated advective transport, as well as bedload transport into account. The water motion is only forced with M_2 tidal constituents. Panel (a) shows WD_{min}, the minimum water depth of equilibrium bed profiles, with its location coded with color. Panel (b) shows the equilibrium bed profiles for three different values of $\Delta\phi_{M_2}$

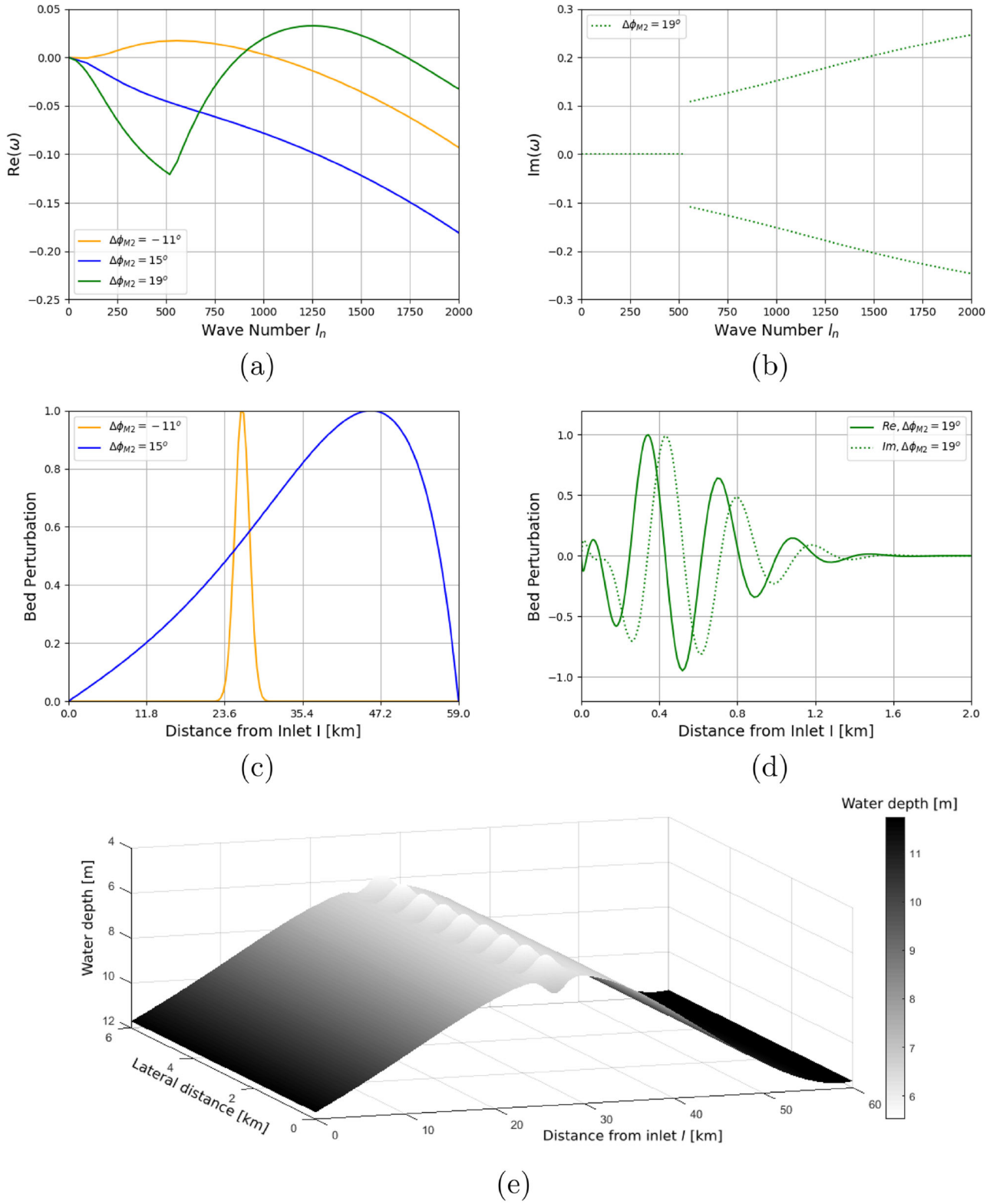

Fig. 3 The dimensionless growth rate $\Re(\omega)$ and, if non–zero, associated imaginary part $\Im(\omega)$ for the most unstable eigenmode (panels (a) and (b), respectively) for $\Delta\phi_{M_2} = -11°$ (orange), $\Delta\phi_{M_2} = 15°$ (blue) and $\Delta\phi_{M_2} = 19°$ (green) as a function of wave number l_n. The corresponding bed patterns (scaled to have a dimensionless amplitude of one for the real part) of the most unstable eigenmodes for the first two phases are shown in panel (c), with the orange solid line the bed pattern associated with $l_n \approx 550$ and $\Delta\phi_{M_2} = -11°$, the blue solid line the pattern for $l_n = 0$ and $\Delta\phi_{M_2} = 15°$. In panel (d), for $\Delta\phi_{M_2} = 19°$, the green solid (dotted) line indicates the real (imaginary) part of the complex bed eigenfunction with mode number $l_n \approx 1200$. Panel (e) shows the spatial structure of the bed perturbation for $\Delta\phi = -11°$

Fig. 3e. Here, a width of $B = 6$ km is used, resulting in $n = 18$. This results in formation of channels and shoals close to the middle of the inlet system. Note that, since only a linear stability analysis is performed, the amplitude used for the bed perturbation is arbitary.

- $\Delta\phi_{M_2} = 15°$ (blue lines in Fig. 3): all eigenvalues of the most unstable mode are again real. However, in contrast to the previous case, all eigenpatterns have a negative growth rate, indicating that the underlying laterally uniform equilibrium bed is linearly stable. The solid blue line in Fig. 3c shows the longitudinal structure of the bed perturbation associated with the $l_n = 0$ eigenmode.
- $\Delta\phi_{M_2} = 19°$ (green lines in Fig. 3): for this relative phase, the eigenvalues of the most unstable eigenmode are real for $0 \leq l_n \lesssim 500$. When $l_n \sim 500$, two complex–conjugated eigenmodes, characterised by complex eigenvalues that are complex conjugates of each other, become the most unstable ones. The real part of these complex eigenvalues is positive for $850 \lesssim l_n \lesssim 1750$, whereas the absolute values of the imaginary parts increase for increasing l_n. In Fig. 3d the real (solid green) and imaginary (dashed green) parts of the most unstable bed pattern are shown. The bottom patterns are found near inlet I, and are very localized: their spatial extent is $\sim$2 km, and the associated bed variations have multiple crests and troughs.

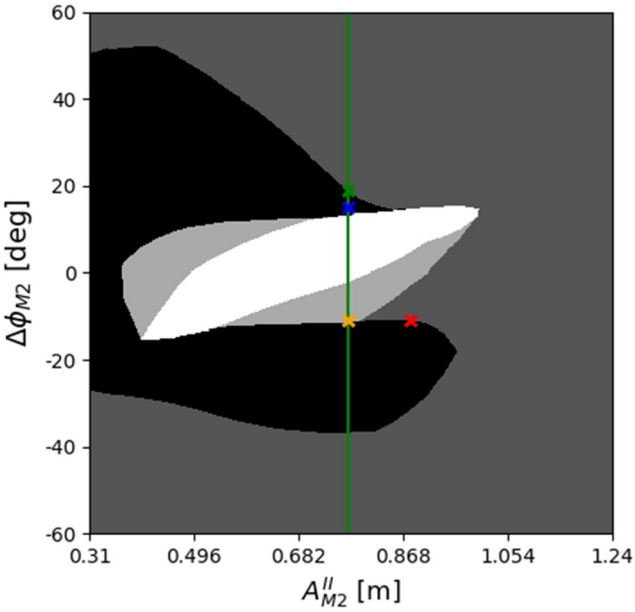

Fig. 4 Existence and linear stability of stable laterally uniform morphodynamic equilibria as a function of the M_2 tidal amplitude at inlet *II* (horizontal axis) and the relative phase (vertical axis). The white, black, dark–gray and light–gray region indicate where no, linearly stable, diffusively unstable and advectively unstable morphodynamic equilibria are found, respectively. If the underlying equilibrium is unstable, the mechanism resulting in the largest positive growth rate is used as indicative of the instability mechanism. The crosses indicate the experiments discussed in detail in the main text

From the above, it follows that the linear stability of 1D–stable laterally uniform equilibria strongly depends on the relative phase difference $\Delta\phi_{M_2}$. In Fig. 4 this dependency on the external M_2 forcing is further illustrated by analysing the linear stability as a function of $A^{II}_{M_2}$ and $\Delta\phi_{M_2}$. In this figure, the region in parameter space where no laterally uniform morphodynamic equilibrium exists is indicated by the white color, linearly stable equilibria are found in the black colored area. In both the dark and light gray colored areas, the laterally uniform morphodynamic equilibria are linearly unstable. The mechanisms resulting in this instability turn out to be diffusively dominated in the light gray area, whereas advective processes are essential in the dark gray region.

To illustrate the two instability mechanisms, we again consider the results obtained with $\Delta\phi_{M_2} = -11°$ and $\Delta\phi_{M_2} = 19°$ with the default A_{M_2} amplitudes, as the first parameter setting results in instabilities due to a diffusive mechanism, while the latter one becomes unstable due to an advective mechanism.

4.1.1 Diffusively dominated instability mechanism

To illustrate the instability mechanisms, we consider the divergence of the various transport contributions for the relative phase $\Delta\phi_{M_2} = -11°$ and $l_n \sim 550$. The longitudinal bed profile of the most unstable eigenfunction is shown in Fig. 3c, orange line. The associated divergences of the classical diffusive flux $<\mathbf{F}^{00}_{\text{diff}}>$, the topographically induced diffusive flux $<\mathbf{F}^{00}_{\text{topo}}>$, the internally generated advective flux $<\mathbf{F}^{20}_{\text{adv}}>$ and the total flux $<\mathbf{F}>$, evaluated at $y = 0$, are shown in Fig. 5a. The classical diffusive transport is destabilizing, i.e., these transports result in a convergence near the tops of the bed perturbation, while the topographically induced diffusive transport is stabilizing with divergence of the transport at the maxima of the bed perturbation. These two transport terms are much bigger than the other two contributions, and they almost balance. To see the net diffusive effect, the divergence of the total diffusive transport defined as $\nabla \cdot (<\mathbf{F}^{00}_{\text{diff}}> + <\mathbf{F}^{00}_{\text{topo}}>)$ is compared with the divergence of the internally generated advective and total transport in Fig. 5b. This illustrates that the combined contribution of the different diffusive transport terms is still dominant, the advective contribution only modifies the divergence of the total transport. Hence the instability mechanism is a *diffusive* one (This observation is corroborated by experiments in which only diffusive transport is considered: similar eigenpatterns, resulting from the same instability mechanism, are found, see Appendix A, Fig. 12). The underlying physical

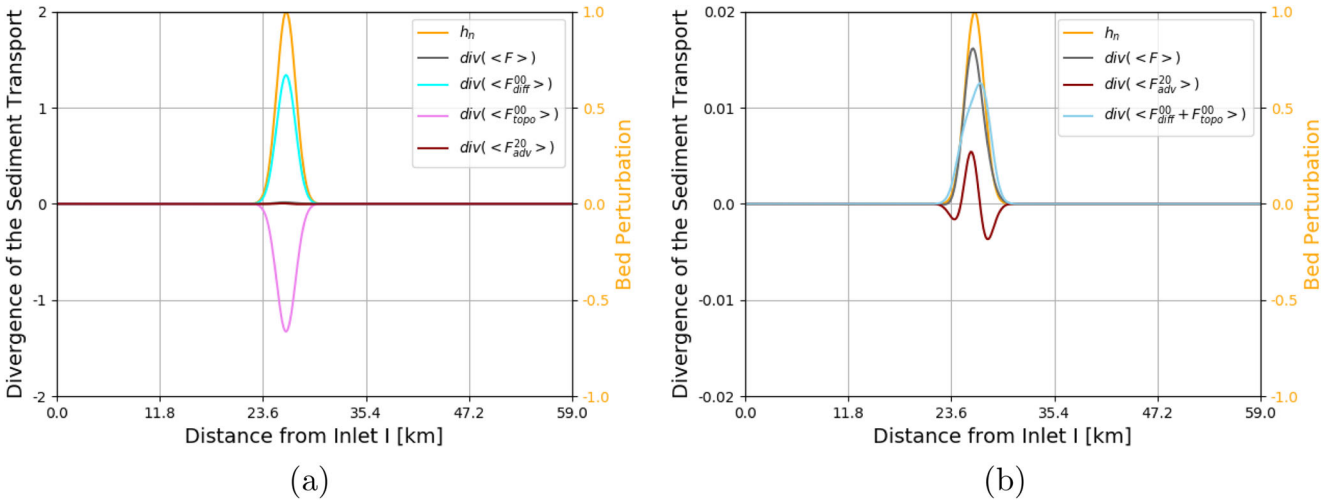

Fig. 5 Dimensionless divergences of the various transport contributions for $\Delta\phi_{M_2} = -11°$ and $l_n \sim 550$, together with the associated bed perturbation (orange line) at $y = 0$. Panel (a) shows all divergences separately, while in Panel (b) the two diffusive contributions are combined

mechanism is described in detail in Schuttelaars and De Swart (1999) with the topographically induced diffusive transport taking over the role of bedload transport (see also Hepkema et al. (2019) and Appendix A).

Whether a bed perturbation is linearly stable or unstable strongly depends on the lateral wave number l_n considered, see the linear stability curve in Fig. 3a: for stable (unstable) eigenfunctions, the stabilizing effects of the divergences of the topographically induced transports dominate over (are dominated by) those of the destabilizing classical diffusive ones.

4.1.2 Advectively dominated instability mechanism

The eigenvalue for the case with $\Delta\phi_{M_2} = 19°$ and $l_n \sim 1200$ is complex, see Fig. 3a and b. This implies that also the eigenfunction consists of a real and an imaginary part. The real and imaginary part of the most unstable bed perturbation is plotted in, respectively, the top and bottom rows of Fig. 6 as the green solid and green dotted lines. In Fig. 6a and c the associated divergences of the various transport terms are shown. As in the previous case, the convergences of diffusive transports are dominant and approximately balance each other. The relative importance of the divergences of the advective and total transports is larger in this case than in the case discussed in Section 4.1.1. Again, by taking the diffusive transports together, we can focus on the relative importance of the diffusive and advective contributions to the total divergence, see Fig. 6b and d. From these figures, it follows that the divergences of the advective transport are larger than those of the total diffusive transport, and is very similar to the divergence of the total transport. This suggests that the instabilities are mainly driven by advective processes, hence the instability mechanism is *advective*. This is confirmed by the experiments discussed in Appendix A: in these experiments the advective transports were not taken into account and the instabilities observed in the present section were not found.

It should also be noted that the divergences associated with the real and imaginary parts of the eigenfunction are out of phase with the bed pattern, associated with this eigenfunction. This is consistent with the fact that these bed patterns do not only grow in time, but are also periodic in time, with the period given by $\Im(\omega)$.

The location where the most unstable eigenpatterns have appreciable amplitudes coincides with a local minimum in water depth of the underlying width–averaged equilibrium. In the previous example, the minimum in water depth was found at inlet I, and the linearly most unstable mode was also observed close to that inlet. When changing the parameters to $A^{II}_{M_2} = 0.87$ m and $\Delta\phi_{M_2} = -11°$, indicated by the red cross in Fig. 4, the underlying morphodynamic equilibrium has a local minimum in water depth at 30 km from inlet I, see Fig. 7a. This laterally uniform equilibrium is linearly unstable, see Fig. 7b, with the spatial structure of the bed pattern associated with the most unstable eigenmode ($l_n \sim 470$) shown in Fig. 7c. The instability mechanism is still dominated by convergences of the internally generated advective transports (not shown). The largest amplitudes of the eigenfunctions are also found at 30 km from inlet I, coinciding with a local minimum in water depth of the underlying morphodynamic equilibrium.

4.2 All forcings included

In this section, the water motion is forced by both the M_2 and M_4 tidal constituents, prescribed at each inlet, and a

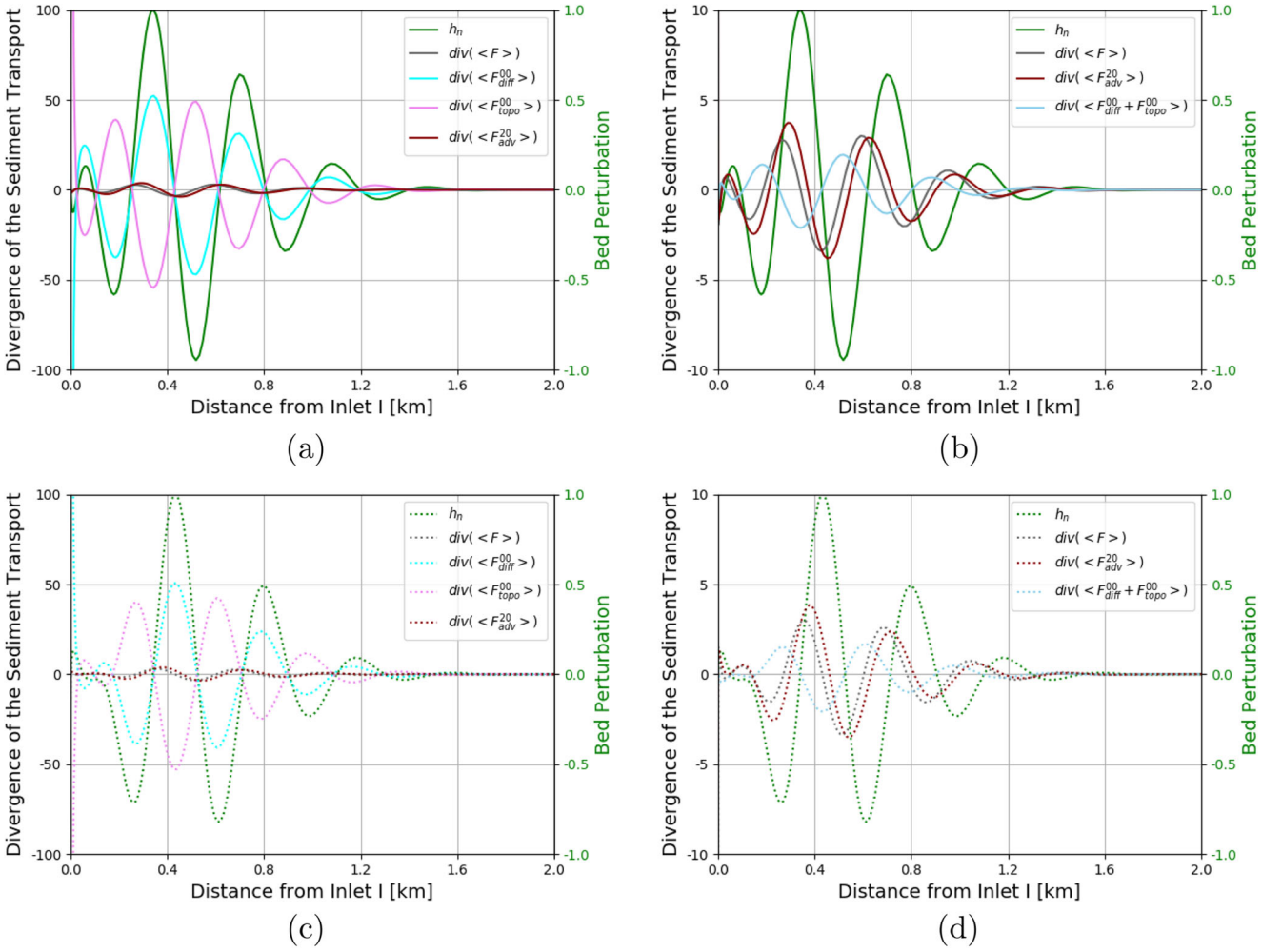

Fig. 6 Dimensionless divergences of the various transport contributions for $\Delta\phi_{M_2} = 19°$ and $l_n \sim 1200$, together with the associated bed perturbation (green line) at $y = 0$. Panels (a) and (c) show the real and imaginary part of the divergences separately, while in Panels (b) and (d) the two diffusive contributions are combined

discharge Q at inlet *II*. Since all forcings are included, all contributions in the bottom evolution equation (18) have to be taken into account when calculating the morphodynamic equilibria and their linear stability.

In this section the influence of the relative M_2 phase $\Delta\phi_{M_2}$ on the stability of the underlying width–averaged equilibria is investigated by changing the M_2 phase at inlet *II*. All other parameters have their default values, see Table 2. To assess this influence, first the associated laterally uniform morphodynamic equilibria have to be obtained. Similar to the experiments in Section 4.1, this is done using a continuation technique, which results in the bifurcation diagram shown in Fig. 8a. In this figure, the minimum water depth of the morphodynamic equilibria is shown as a function of $\Delta\phi_{M_2}$. In the interval $5° \lesssim \Delta\phi_{M_2} \lesssim 25°$ no morphodynamic equilibria exist for which the two inlets are connected. For $-60° \leq \Delta\phi_{M_2} \lesssim 5°$ and $25° \leq \Delta\phi_{M_2} \leq 60°$ two morphodynamic equilibria are found, one 1D–stable (solid line) and the other one 1D–unstable (dashed line).

The two–dimensional stability of the 1D–stable equilibria depends on $\Delta\phi_{M_2}$. For values of $\Delta\phi_{M_2}$ between $-17°$ and $3°$, the 1D–stable equilibria are also linearly stable against two–dimensional perturbations (not shown). For all other $\Delta\phi_{M_2}$, the laterally uniform equilibria that were 1D–stable turn out to be linearly unstable against two–dimensional perturbations (not shown). All instabilities are advectively dominated, with transport due to both internally generated and externally prescribed advection being important. To illustrate this, we consider $\Delta\phi_{M_2} = 31°$. The associated equilibrium bed profile is shown in Fig. 8b. The real and imaginary part of the eigenvalues are shown in Fig. 8c. From this figure it follows that eigenfunctions with lateral wave number l_n between 400 and 2750 have a positive growth rate, with a maximum growth rate found for $l_n \sim 1100$. This maximum growth rate increases very

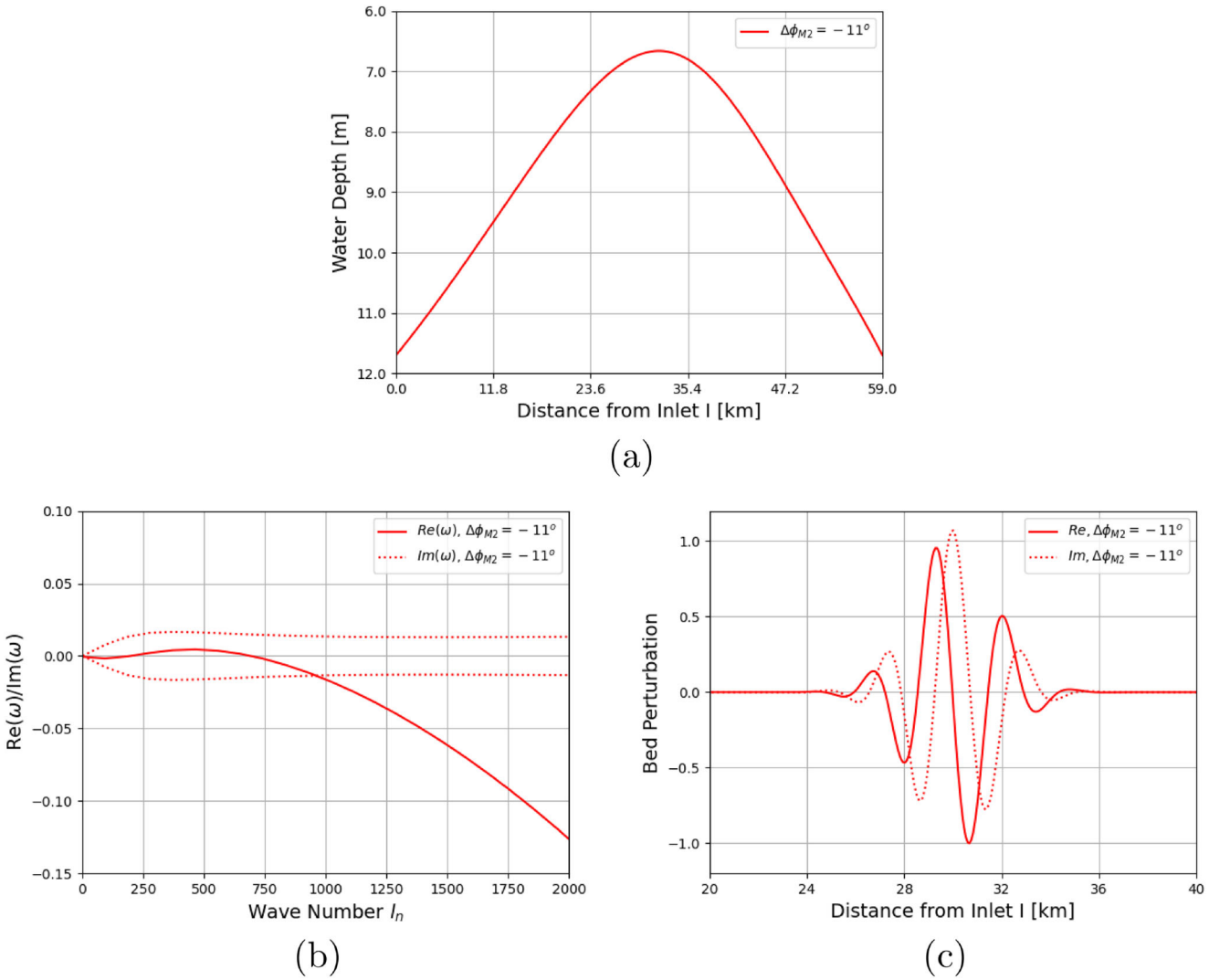

Fig. 7 (a) Laterally uniform morphodynamic equilibrium obtained with $A^{II}_{M_2} = 0.87$ m and $\Delta\phi_{M_2} = -11°$, (b) the real and imaginary parts of the eigenvalue associated with the most unstable eigenfunction as a function of the lateral wave number and (c) the bed pattern of the most unstable eigenfunction

quickly for increasing $\Delta\phi_{M_2}$ and is associated with ever increasing lateral mode number (not shown). The real and imaginary part of the associated eigenfunction is shown in Fig. 8d, illustrating that the bed perturbation is found close to inlet I.

In Fig. 9 the various contributions to the real (panels a and b) and imaginary (panels c and d) part of the divergence of the suspended sediment transports are shown. As observed in Section 4.1, the diffusive contributions dominate when considered separately, but when adding them together all contributions are of the same order of magnitude. From Fig. 9b and d it follows that the total diffusive transports $< \mathbf{F}^{00}_{\text{diff}} > + < \mathbf{F}^{00}_{\text{topo}} >$ and the advective transport due to external overtides $< \mathbf{F}^{11}_{\text{adv}} >$ are in phase, except near the entrance where $< \mathbf{F}^{11}_{\text{adv}} >$ dominates the transport. All contributions are of the same order of magnitude, indicating that the advective transport mechanism, due to both internally generated and externally prescribed overtides, is important for these instabilities.

5 Discussion and conclusions

In this paper, we show that stable laterally uniform morphodynamic equilibria of rectangular double inlet systems can become linearly unstable when two dimensional perturbations are considered, resulting in the formation of channels and shoals as a result of a positive feedback mechanism between the tidal flow and the bottom. The water motion is described by the shallow water equations, neglecting Coriolis terms, and driven by M_2 and M_4 tidal constituents, prescribed at both connections to the sea, and by a

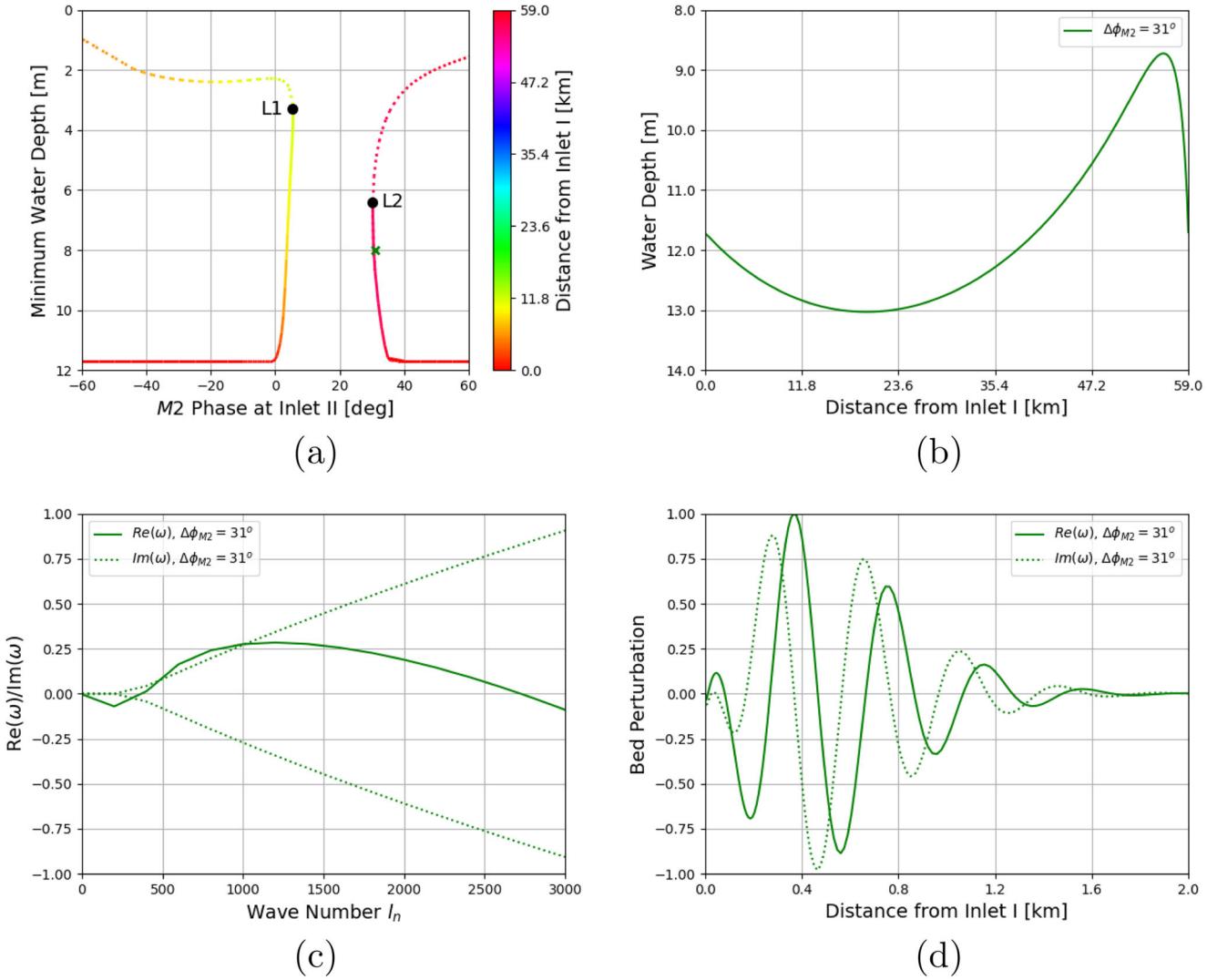

Fig. 8 Panel (a) shows WD_{min}, the minimum water depth of laterally uniform equilibrium bed profiles, with the location of WD_{min} color–coded. Panel (b) shows the laterally uniform equilibrium bed profile for $\Delta\phi_{M_2} = 31°$, (c) the real and imaginary parts of the eigenvalue associated with the most unstable eigenfunction as a function of the lateral wave number and (d) the bed perturbations of the most unstable eigenfunction

constant discharge, prescribed at one of the inlets. Sediment is transported both as suspension load due to advective and diffusive processes and as bedload due to bedslope effects. Since the tidal time scale is much shorter than the morphodynamic time scale, the method of averaging is applied to separately describe the dynamics of the water motion and the bottom. Owing to the assumption of a rectangular inlet system, no direct comparison can be made with observations of real world systems. However, valuable insights are gained in better understanding the various mechanisms resulting in instabilities in double inlet systems.

When the water motion is only forced by an M_2 tidal constituent, both advective and diffusive processes result in tidally averaged suspended sediment transports. The advective transport is the result of nonlinear interactions of the directly forced signals. Considering the diffusive suspended sediment transport, two different sediment transport mechanisms are identified: the classical one (related to spatial gradients in the depth–integrated tidally–averaged suspended sediment concentrations) and the topographically induced suspended sediment transport (associated with gradients in the bed level). Keeping the amplitude and phase of the M_2 tidal forcing at one inlet fixed, and varying these parameters for the other inlet, it is found that there is an area in the amplitude–phase plane where no laterally uniform morphodynamic equilibria exist for which both inlets are still connected. In the parameter space where such equilibria exist, the equilibrium can be stable against two–dimensional perturbations, linearly unstable due to convergences of

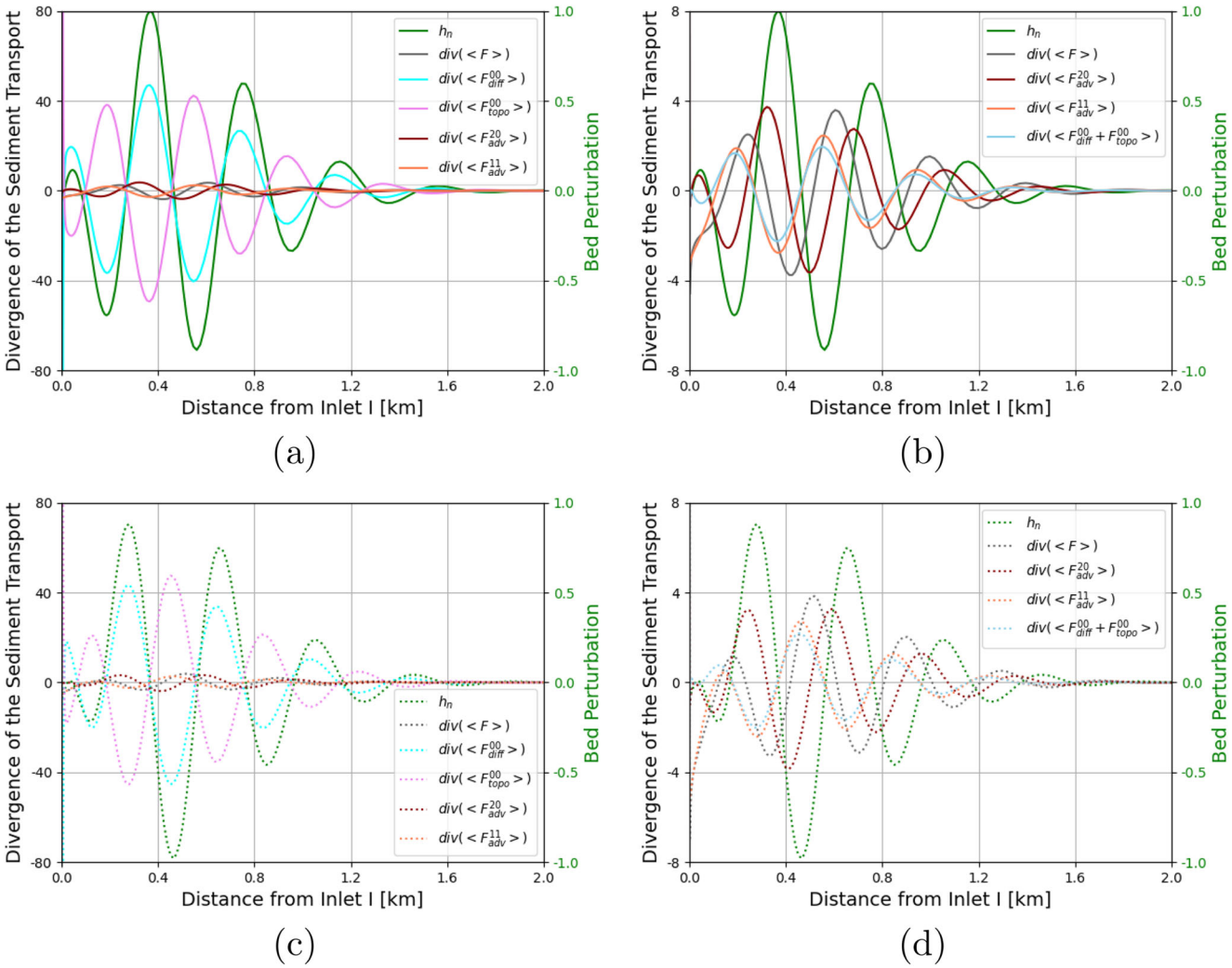

Fig. 9 Dimensionless divergences of the various transport contributions for $\Delta\phi_{M_2} = 31^\circ$ and $l_n \sim 1100$, together with the associated bed perturbation (green line) at $y = 0$. Panels (a) and (c) show the real and imaginary part of the divergences separately, while in Panels (b) and (d) the two diffusive contributions are combined

diffusive transport mechanisms, or linearly unstable due to convergences related to advective processes.

When the morphodynamic equilibrium becomes unstable due to diffusive processes, the classical diffusive mechanism destabilizes laterally uniform morphodynamic equilibria, while the mechanism related to topographic gradients has a stabilizing effect. The relative importance of these mechanisms determines whether the laterally uniform equilibrium is linearly stable or instabilities start to grow. This instability mechanism is similar to the one described by Schuttelaars and De Swart (1999) and Ter Brake and Schuttelaars (2011) for single–inlet systems. The eigenvalues are all real, implying an exponential growth in time. When advective transport mechanisms result in linear instabilities, the eigenvalues are found to be complex–valued. This implies that bedforms do not only grow in time, but also migrate. In this case convergences and divergences of both advective and diffusive transports contribute significantly to the linear growth of the bed perturbations.

When including external overtides and a residual discharge, the influence of the relative M_2 phase between the M_2 forcing at the two inlets is investigated, using default values for all other parameters. It was found that there are either no morphodynamic equilibria that connect both inlets or that these equilibria are unstable due to the convergences and divergences of both advective and diffusive transports which are of equal importance. Here, the advective transports are a result of internally generated overtides and due to the prescribed external overtide and discharge.

It is found that in all cases the bed perturbations have their largest amplitudes in the regions where the water depth of the underlying morphodynamic equilibrium

has a local mimimum. This observation is in line with the remark in Schuttelaars and De Swart (1999) that a necessary condition for instability is the presence of bottom frictional torques. In the present model, a similar obervation can be made: when reducing the friction parameter below a critical value, the underlying laterally uniform morphodynamic equilibrium is always stable (not shown). Only by introducing the effects of bottom friction, the underlying equilibria become unstable, both when the convergence of the sediment transport is dominated by diffusive and advective mechanisms.

The linear instabilities found in this paper result in the initial formation of channels and shoals in the shallower regions of the tidal basin system. The location of initial formation coincides with results obtained in numerical models and laboratory experiments (Hibma et al. 2003; Van der Wegen and Roelvink 2008; Leuven and Kleinhans 2019). To compare results beyond the initial stage of channel–shoal formation, a nonlinear analysis has to be performed, which is the topic of a subsequent study.

Appendix A: Diffusively dominated transport

The influence of the relative M_2 phase, $\Delta\phi_{M_2}$, on the diffusively dominated morphodynamic equilibria is investigated. For simplicity, the undisturbed water depth at inlet *II* is taken to be equal to 11.7 m, the same water depth as inlet *I*. All other parameter values are taken from Table 2. When the sediment transport is dominated by diffusion, the morphodynamic equilibrium condition reduces to

$$\nabla \cdot \left(<\mathbf{F}^{00}_{\text{diff}}> + <\mathbf{F}^{00}_{\text{topo}}> + <\mathbf{F}_{\text{bed}}> \right) = 0. \tag{A1}$$

In a rectangular geometry, morphodynamic equilibria which are laterally uniform can be found using the bifurcation approach discussed in Deng et al. (2021). As an example, Fig. 10a shows the minimum water depths WD_{min} of these morphodynamic equilibria as a function of $\Delta\phi_{M_2}$ varying from $-60°$ to $60°$. It demonstrates that the existence of morphodynamic equilibria depends on the relative M_2 phase: for $\Delta\phi_{M_2}$ between $10°$ to $16°$, no morphodynamic equilibrium is found for which both inlets are connected. For other relative M_2 phases considered, there is always a 1D–stable equilibrium.

To investigate the linear stability of these 1D–stable morphodynamic equilibria to the perturbations with lateral structure, morphodynamic equilibria obtained with $\Delta\phi_{M_2} = 19°$ (orange), $\Delta\phi_{M_2} = 20°$ (green) and $\Delta\phi_{M_2} = 25°$ (red) are examined. Their bed profiles are shown in Fig. 10b. These three equilibrium bed profiles correspond to WD_{min} indicated by crosses (with colors associated to their bed profiles) in Fig. 10a. The largest dimensionless growth rate $\Re(\omega)$ of these three morphodynamic equilibria as a function of dimensionless wave number l_n is shown in Fig. 11a. It shows that at $l_n = 0$ the largest dimensionless growth rate $\Re(\omega)$ is negative for all three selected $\Delta\phi_{M_2}$, which shows these three morphodynamic equilibria

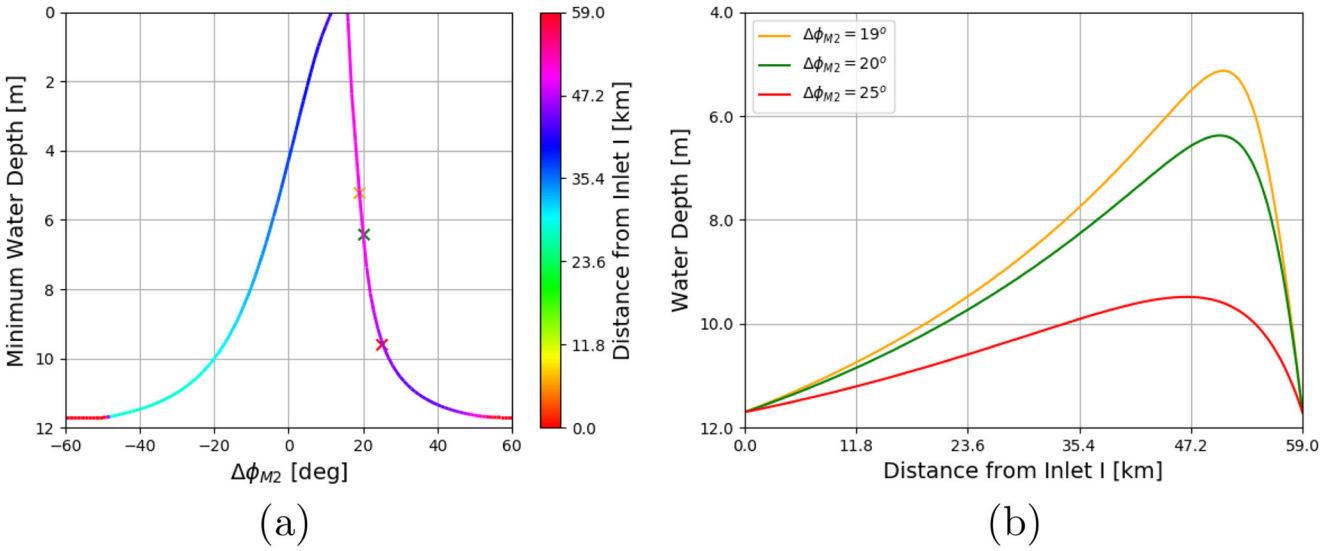

Fig. 10 Laterally uniform morphodynamic equilibria for diffusively dominated transport. Panel (a) shows WD_{min} the minimum water depth of equilibrium bed profiles, with its location coded with color. Panel (b) shows the equilibrium bed profiles for three different values of $\Delta\phi_{M_2}$. The minimum water depths in the cases shown in panel(b) are indicated by cross-shaped markers in panel (a)

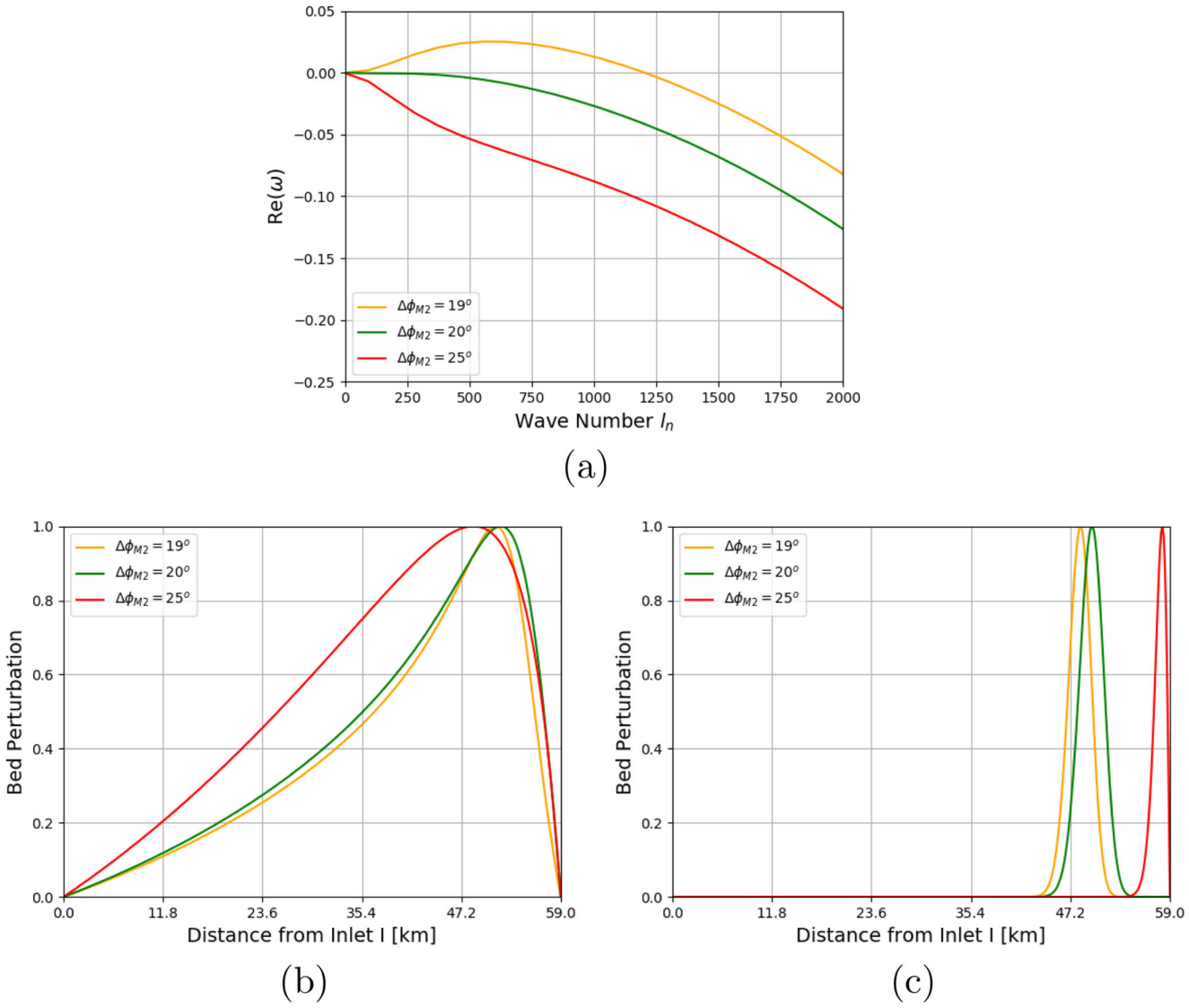

Fig. 11 The dimensionless growth rate $\Re(\omega)$ for three different $\Delta\phi_{M_2}$ (Panel (a)). The corresponding bottom patterns h_n for mode number $n = 0$ ($l_n = 0$) are shown in panel (b), while those for mode number $n = 18$ ($l_n = 555.9$) are shown in panel (c)

are 1D–stable. Increasing the dimensionless wave number l_n from 0 to 1200, the largest dimensionless growth rate $\Re(\omega)$ for $\Delta\phi_{M_2} = 19°$ first increases, till a maximum is obtained at approximately $l_n = 560$, and then decreases to become negative for $l_n \sim 1200$. Positive $\Re(\omega)$ indicates that the laterally uniform morphodynamic equilibrium for $\Delta\phi_{M_2} = 19°$ is unstable against perturbations with a lateral structure. Unlike $\Delta\phi_{M_2} = 19°$, the largest dimensionless growth rate $\Re(\omega)$ for $\Delta\phi_{M_2} = 25°$ is negative for all l_n considered, which indicates the corresponding equilibrium is stable against perturbations with lateral structure. The critical value of the relative M_2 phase, $\Delta\phi_{M_2}$, that seperates stable and unstable morphodynamic equilibrium against perturbations with lateral structure, is $\Delta\phi_{M_2} = 20°$ (see also Fig. 14).

When using width $B = 6\ km$, the dimensionless wave number $l_n = 555.9$, at which $\Re(\omega)$ for $\Delta\phi_{M_2} = 19°$ reaching a maximum, corresponds to a mode number $n = 18$. The bed patterns h_n for $n = 18$ ($l_n = 555.9$) are shown in Fig. 11c. Compared with the bed patterns for $n = 0$ shown in Fig. 11b, the bed patterns for $n = 18$ are more localized, i.e., the bed patterns for $n = 18$ are nonzero within a region of approximately $15km$, while the bed patterns for $n = 0$ are nonzero everywhere between the two inlets. Figure 11c also shows that the bed patterns for $n = 18$ are close to where $\mathrm{WD}_{\mathrm{min}}$ is found. The

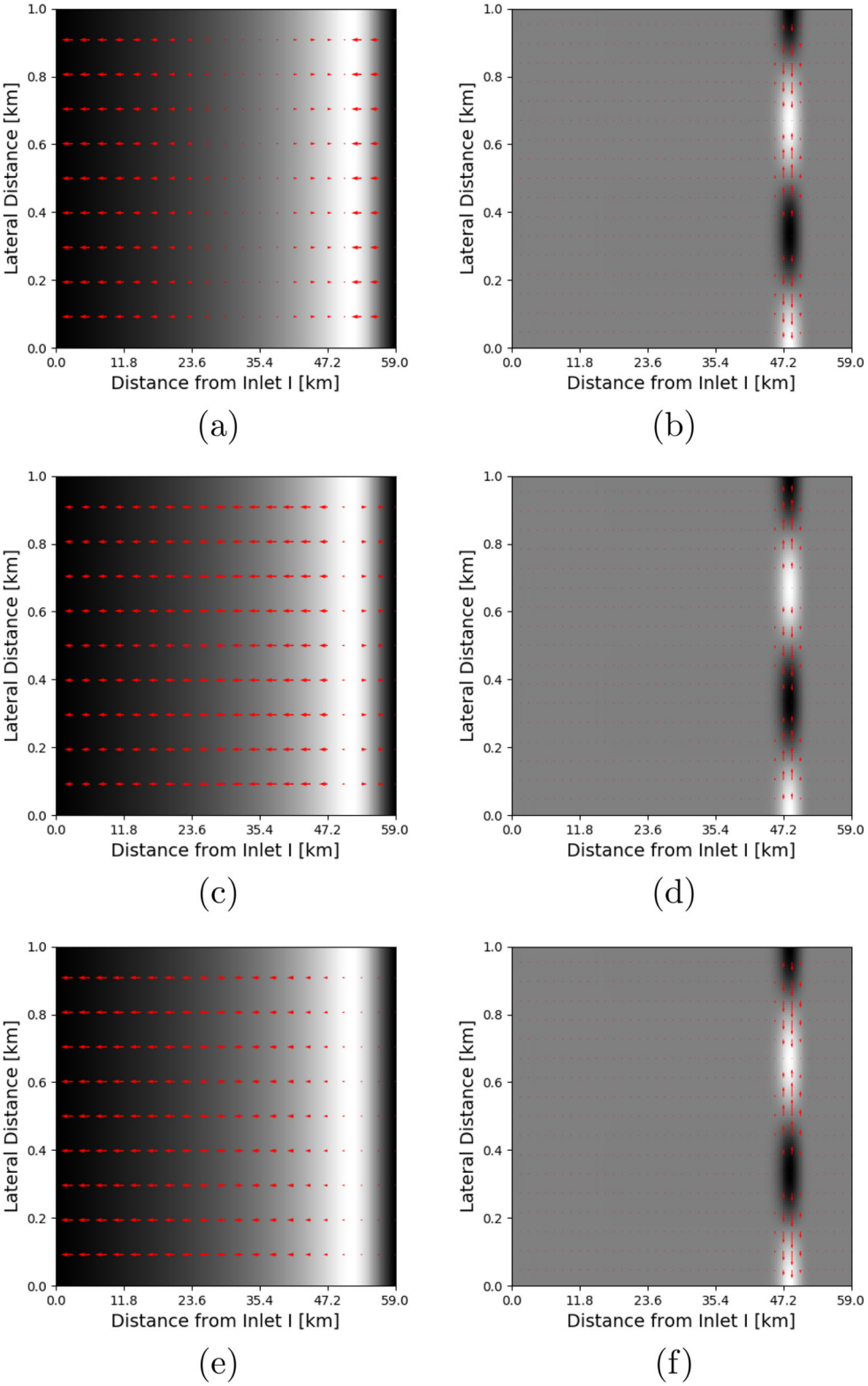

Fig. 12 Bottom patterns of laterally uniform morphodynamic equilibria for diffusively dominated transport. Panels (a), (c) and (e) show the bottom patterns for $\Delta\phi_{M_2} = 19°$ and $n = 0$, with white areas representing crests and dark areas representing troughs. The arrows indicate the direction and relative magnitude of classical diffusive flux $<\mathbf{F}^{00}_{\text{diff}}>$, the topographically induced diffusive flux $<\mathbf{F}^{00}_{\text{topo}}>$ and the total flux $<\mathbf{F}>$. Panels (b), (d) and (f) show the same but for $\Delta\phi_{M_2} = 19°$ and $n = 18$

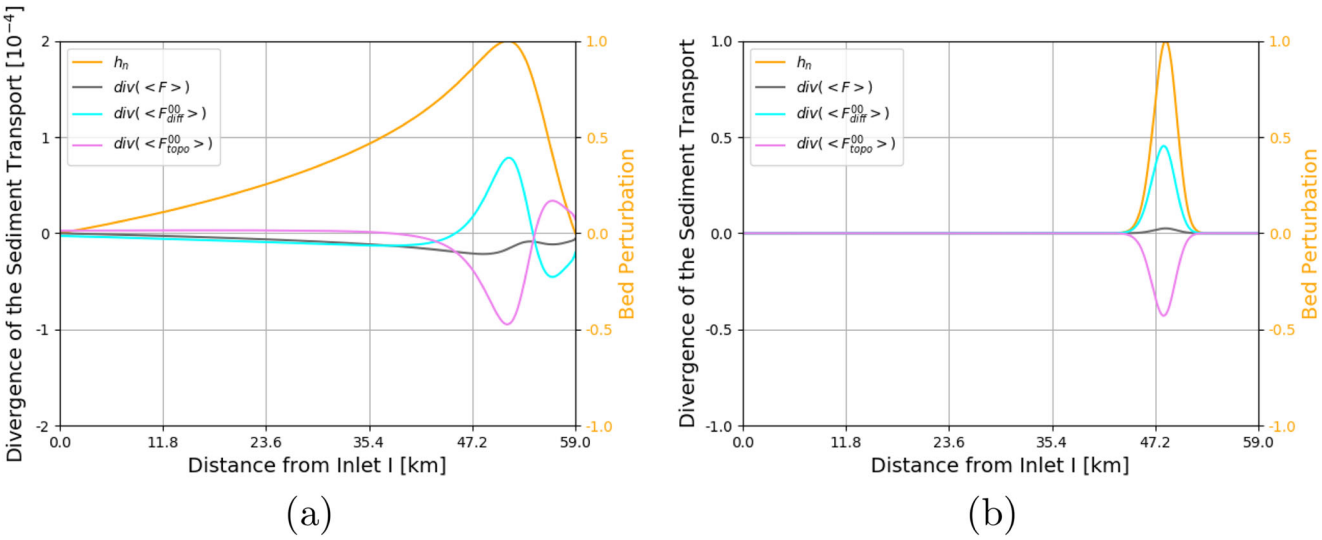

Fig. 13 Divergences of sediment fluxes. Panel (a) shows the divergences of the sediment fluxes for $\Delta\phi_{M_2} = 19°$ and mode number $n = 0$ at $y = 0$, together with the corresponding bottom pattern. Panel (b) shows the same but for $\Delta\phi_{M_2} = 19°$ and mode number $n = 18$

morphodynamic equilibrium for $\Delta\phi_{M_2} = 19°$ is called diffusively unstable, since only diffusive transport plays a role.

To study the instability mechanism in detail, the classical diffusive transport $< \mathbf{F}^{00}_{\text{diff}} >$, the topographically induced diffusive transport $< \mathbf{F}^{00}_{\text{topo}} >$ and the total transport $< \mathbf{F} >$ of the first 1 km in lateral direction for $\Delta\phi_{M_2} = 19°$ and mode number $n = 0$ are shown in Fig. 12a, c and e, while those for $\Delta\phi_{M_2} = 19°$ and mode number $n = 18$ are shown in Fig. 12b, d and f, respectively. These figures show that the topographically induced diffusive transport $< \mathbf{F}^{00}_{\text{topo}} >$ is directed from crests to troughs and stablizes the bottom pattern, while the classical diffusive transport $< \mathbf{F}^{00}_{\text{diff}} >$ is generally directed from troughs to crests and destablizes the bottom patterns. These two diffusive transport result in a total transport $< \mathbf{F} >$, which can be either directed from crests to troughs ($n = 0$) or from troughs to crests ($n = 18$), depending on the mode number n, as well as the relative M_2 phase. When mode number $n = 0$, these three sediment transports flow in a longitudinal direction, since there is no lateral structure, while these transports flow laterally when mode number $n = 18$.

The instability mechanism can also be studied using the divergences of these three sediment fluxes, which have the same lateral structure as their corresponding bottom pattern. Figure 13a shows these divergences in the longitudinal direction at $y = 0$ for $\Delta\phi_{M_2} = 19°$ and mode number $n = 0$, together with the corresponding bottom pattern, while the ones for $\Delta\phi_{M_2} = 19°$ and mode number $n = 18$ are shown in Fig. 13b. From these figures it follows that the divergence of the classical diffusive transport $< \mathbf{F}^{00}_{\text{diff}} >$ enhances perturbations of bottom patterns, and the divergence of topographically induced diffusive transport $< \mathbf{F}^{00}_{\text{topo}} >$ reduces the amplitudes of the perturbations. These two sediment transports almost balance each other, resulting in a divergence of the total transport $< \mathbf{F} >$ with smaller magnitude. When mode number $n = 0$ is considered, $< \mathbf{F} >$ transports sediment from troughs to crests, while for mode

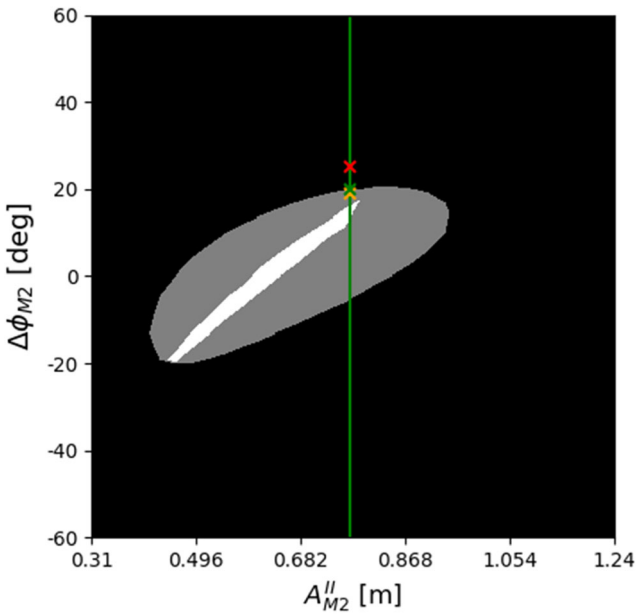

Fig. 14 Existence and linear stability of stable laterally uniform morphodynamic as a function of the M_2 tidal amplitude at inlet II and the raltive phases when dominated by diffusive transport. The white, black, dark region indicate where no, linearly stable, diffusively unstable morphodynamic equilibria are found. If the underlying equilibrium is unstable, the mechanism resulting in the largest positive growth rate is used as indicateive of the instability mechanism. The crosses indicate the experiments discussed in detail in this Appendix A

number $n = 18$, $<\mathbf{F}>$ transports sediment from crests to troughs.

The existence and stability of laterally uniform morphodynamic equilibria depends not only on the relative M_2 phase but also on the M_2 amplitude at inlet $I\!I$, which is shown in Fig. 14. In this figure, the region in parameter space where no laterally uniform morphodynamic equilibrium exists, is indicated by the white color. Linearly stable equilibria are found in the black colored area, while linearly unstable equilibria (resulting from the diffusive mechanism) in the light gray colored area.

Declarations

Data sharing not applicable to this article as no datasets were generated or analysed during the current study.

This article is financially supported by the China Scholarship Council (nr. 201706890036).

Conflict of Interests The authors report no conflict of interest.

References

Csanady GT (1982) Circulation in the Coastal Ocean, Reidel, Boston

D'Alpaos A, Lanzoni S, Marani M et al (2007) Landscape evolution in tidal embayments: modelling the interplay of erosion, sedimentation, and vegetation dynamics. J Geophys Res 112:F01,008

Dalrymple RW, Rhodes RN (1995) Chapter 13 estuarine dunes and bars. In: Perillo G (ed) Geomorphology and sedimentology of estuaries, developments in sedimentology, vol 53. Elsevier, pp 359–422. https://doi.org/10.1016/S0070-4571(05)80033-0. https://www.sciencedirect.com/science/article/pii/S0070457105800330

De Swart HE, Zimmerman JTF (2009) Morphodynamics of tidal inlet systems. Ann Rev Fluid Mech 41:203–229

Deng X, Meerman C, Boelens T et al (2021) Morphodynamic equilibria in double–inlet systems: existence and stability. J Geophys Res 126:2021JF006,266

Duran-Matute M, Gerkema T, De Boer GJ et al (2014) Residual circulation and freshwater transport in the dutch wadden sea: a numerical modelling study. Ocean Sci 10:611–632

Dyer KR (1986) Coastal and estuarine sediment transport. Wiley, Chichester, p 342

Falqués A, Montoto A, Iranzo V (1996) Bed–flow instability of the longshore current. Cont Shelf Res 15:1927–1964

Glaeser DJ (1978) Global distribution of barrier islands in terms of tectonic setting. J Geol 86:283–297

Hepkema T, De Swart H, Schuttelaars H (2019) The sensitivity of tidal bar wavelength to channel width. J Geophys Res Earth Surf 124:2417–2436

Hibma A, De Vriend HJ, Stive MJF (2003) Numerical modelling of shoal pattern formation in well-mixed elongated estuaries. Estuar Coast Shelf Sci 57:981–991

Hibma A, Schuttelaars HM, De Vriend HJ (2004) Initial formation and evolution of channel-shoal patterns in estuaries. Cont Shelf Res 24:1637–1650

Israel CG, Dunsbergen DW (2000) Cyclic morphological development of the ameland inlet, the Netherlands. River, Coastal and Estuarine Morphodynamics 1:701–714

Krol M (1991) On the averaging method in nearly time-periodic advection-diffusion problems. SIAM J Appl Math 51:1622–1637

Leuven J, Kleinhans M (2019) Incipient tidal bar and sill formation. J Geophys Res: Earth Surface 124(7):1762–1781. https://doi.org/10.1029/2018JF004953

Lorentz H (1922) Het in rekening brengen van den weerstand bij schommelende vloeistofbewegingen. De Ingenieur, p 695

Marciano R, Wang Z, Hibma A et al (2005) Modeling of channel patterns in short tidal basins. J Geophys Res 110. https://doi.org/10.1029/2003JF000092

McBride RA, Byrnes MR, Hiland MW (1995) Geomorphic response-type model for barrier coastlines: a regional perspective. Mar Geol 126:143–159

Meerman C, Rottschäfer V, Schuttelaars H (2019) Influence of geometrical variations on morphodynamic equilibria in short tidal basins. Ocean Dyn 69(2):221–238. https://doi.org/10.1007/s10236-018-1236-7

Mulhern J, Johnson C, Martin J (2017) Is barrier island morphology a function of tidal and wave regime? Mar Geol 387:74–84. https://doi.org/10.1016/j.margeo.2017.02.016

Oost AP, Hoekstra P, Wiersma A et al (2012) Barrier island management: lessons from the past and directions for the future. Ocean Coast Manag 68:18–38

Pacheco A, Vila-Concejo A, Ferreira O et al (2008) Assessment of tidal inlet evolution and stability using sediment budget computations and hydraulic parameter analysis. Mar Geol 247:104–127

Ridderinkhof H (1988) Tidal and residual flows in the western Dutch Wadden sea i1: an analytical model to study the constant flow between connected tidal basins. Neth J Sea Res 22:185–198

Salles P, Voulgaris G, Aubrey DG (2005) Contribution of nonlinear mechanisms in the persistence of multiple tidal inlet systems. Estuar Coast Shelf Sci 65:475–491

Sanders JA, Verhulst F (1985) Averaging methods in nonlinear dynamical systems. Springer, New York

Sassi M, Duran-Matute M, Van Kessel T et al (2015) Variability of residual fluxes of suspended sediment in a multiple tidal-inlet system: the Dutch wadden sea. Ocean Dyn 65(9-10):1321–1333. https://doi.org/10.1007/s10236-015-0866-2. https://www.scopus.com/inward/record.uri?eid=2-s2.0-849423657%37&doi=10.1007%2fs10236-015-0866-2&partnerID=40&md5=74b84a90302a69c787d42d9fc0%ce8f0b

Schuttelaars HM, De Swart HE (1996) An idealized long-term morphodynamic model of a tidal embayment. Eur J Mech B/Fluids 15:55–80

Schuttelaars HM, De Swart HE (1999) Initial formation of channels and shoals in a short tidal embayment. J Fluid Mech 386:15–42

Schuttelaars HM, De Swart HE (2000) Multiple morphodynamic equilibria in tidal embayments. J Geophys Res 105:105–124

Seminara G, Bolla Pittaluga M, Tambroni N et al (2005) Open problems in modelling the long-term morphodynamic evolution of venice lagoon. Flooding and environmental challenges for Venice and its lagoon, pp 345–353

Stutz ML, Pilkey OH (2011) Open-ocean barrier islands: global influence of climatic, oceanographic, and depositional settings. J Coast Res 27:207–222

Tambroni N, Seminara G (2006) Are inlets responsible for the morphological degradation of venice lagoon? J Geophys Res: Earth Surface 111. https://doi.org/10.1029/2005JF000334. https://www.scopus.com/inward/record.uri?eid=2-s2.0-34147093357&doi=10.1029%2f2005JF000334&partnerID=40&md5=e8c4184e8ee04ee58bfe0449486c0b9b

Ter Brake MC, Schuttelaars HM (2010) Modeling equilibrium bed profiles of short tidal embayment. on the effect of the vertical distribution of suspended sediment and the influence of the boundary conditions. Ocean Dyn 60:183–204

Ter Brake MC, Schuttelaars HM (2011) Channel and shoal development in a short tidal embayment: an idealized model study. J Fluid Mech 677:503–529

Van der Spek AJF (1997) Tidal asymmetry and long-term evolution of holocene tidal basins in the netherlands: simulation of paleo-tides in the scheldt estuaries. Mar Geol 141:71–90

Van Leeuwen SM, De Swart HE (2001) The effect of advective processes on the morphodynamic stability of short tidal embayments. Phys Chem Earth (B) 26:735–740

Van Leeuwen SM, De Swart HE (2004) Effect of advective and diffusive sediment transport on the formation of local and global bottom patterns in tidal embayments. Ocean Dyn 54:441–451

Van der Wegen M, Roelvink JA (2008) Long-term morphodynamic evolution of a tidal embayment using a two-dimensional process-based model. J Geophys Res 7:C03,016. https://doi.org/10.1029/2006JC003983

Zimmerman JTF (1992) On the lorentz linearization of a nonlinearly damped tidal helmholtz oscillator. Proceedings KNAW 95:127–145